JFM PAPERS

Splash on a liquid pool: coupled cavity–sheet unsteady dynamics

R. Dandekar[1,‡], **N. Shen**[1,‡], **B. Naar**[1] **and L. Bourouiba**[1,†]

[1]The Fluid Dynamics of Disease Transmission Laboratory, Fluids and Health Network, Massachusetts Institute of Technology, Cambridge, MA 02139, USA

Splashes from impacts of drops on liquid pools are ubiquitous and generate secondary droplets important for a range of applications in healthcare, agriculture and industry. The physics of splash continues to comprise central unresolved questions. Combining experiments and theory, here we study the sequence of topological changes from drop impact on a deep, inviscid liquid pool, with a focus on the regime of crown splash with developing air cavity below the interface and crown sheet above it. We develop coupled evolution equations for the cavity–crown system, leveraging asymptotic theory for the cavity and conservation laws for the crown. Using the key coupling of sheet and cavity, we derive similarity solutions for the sheet velocity and thickness profiles, and asymptotic prediction of the crown height evolution. Unlike the cavity whose expansion is opposed by gravitational effects, the axial crown rise is mostly opposed by surface tension effects. Moreover, both the maximum crown height and the time of its occurrence scale as $We^{5/7}$. We find our analytical results to be in good agreement with our experimental measurements. The cavity–crown coupling achieved enables us to obtain explicit estimates of the crown splash spatio-temporal unsteady dynamics, paving the way to deciphering ultimate splash fragmentation.

Key words: drops, interfacial flows (free surface), aerosols/atomization

1. Introduction

Impacts of drops on liquid layers are ubiquitous. With sufficient energy, such impacts can lead to a splash, producing myriads of secondary small and fast droplets of great importance to understand environmental processes such as raindrops impacting oil spills on the surface of the ocean (Teal & Howarth 1984; Aguilera *et al.* 2010; Fingas 2013), as well as in healthcare, agriculture and wastewater treatment plants. In these systems,

† Email address for correspondence: lbouro@mit.edu
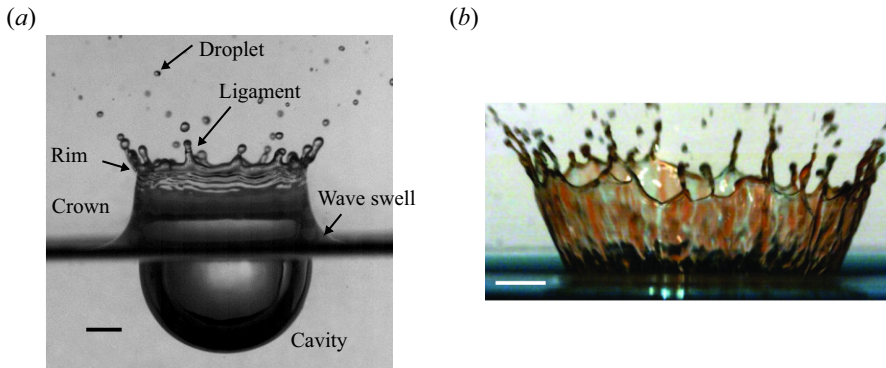‡ Equal contribution.

(a) (b)

Figure 1. (a) Splash on deep pool forming a cavity, wave swell, crown and secondary droplets. The crown is bounded upward by a rim, a bulge, typical of extended free sheets in the air. The rim destabilizes to form the ligaments and droplets seen ejected upward. Scale bar: 2 mm. (b) Splash on a thin film (Bourouiba 2021*a*). The impinging drop liquid and the receiving film liquid are of different colours, showing complex mixing in the ejected droplets. Scale bar: 4 mm.

pathogens, pesticides or a range of contaminants contained in these impacted pools can be released and contribute to air contamination via the splash ejection of carrier droplets and aerosols (Horrocks 1907; Darlow & Bale 1959; Gerba, Wallis & Melnick 1975; Rein 1993; Barker & Jones 2005; Yarin 2006; Johnson *et al.* 2013; Traverso *et al.* 2013; Bourouiba, Dehandschoewercker & Bush 2014; Gilet & Bourouiba 2014, 2015; Josserand & Thoroddsen 2016; Jung *et al.* 2016; Poulain & Bourouiba 2018; Alsved *et al.* 2019; Poulain & Bourouiba 2019; Bourouiba 2021*a*,*b*). In industrial applications, the control of spray, thermal coatings, and more also requires understanding of splash (Aziz & Chandra 2000; Fauchais *et al.* 2004; Dhiman & Chandra 2005).

Upon impact on a pool, a liquid drop of diameter d_0 and impact velocity u_0 can generate a splash (see figure 1). When a splash occurs on a deep pool (figure 1*a*), first, an air cavity forms below the liquid interface while a cylindrical liquid sheet rises above the surface (figure 1). As the sheet rises, azimuthal instabilities emerge, leading to the formation of ligaments themselves breaking into secondary droplets, giving it a crown-like form (figure 1*a*). Upon reaching maximum height, the crown starts to collapse back into the pool. Eventually the cavity collapses as well. During such process a myriad of secondary droplets can be formed and projected with great speed. Moreover, a high-pressure stagnation point can be created in the underlying cavity, forming an upward-rising jet, itself potentially breaking to generate further droplets. The seemingly simple droplet impact on a liquid pool thus shows a rich behaviour. In many applications, the resulting complex mixing between the impinging and receiving liquids is of critical importance. For example, using dyes of different colour, figure 1(*b*) shows that droplets of different liquid compositions can be generated after impact. Since the seminal work of Worthington (Worthington 1877, 1883, 1908; Worthington & Cole 1897) and Edgerton (Edgerton & Killian 1954), the rich physics governing liquid-on-liquid impacts and the resulting splash have been the subject of extended interest.

Depending on the energetics of the impact with respect to the interfacial and gravitational restoring forces, a crown splash can occur (figure 1) or is replaced by a closing cavity eventually forming a bubble and jet (figure 2*a*). The Weber number, *We*, and Froude number, *Fr*, are two non-dimensional parameters quantifying the relative importance of the kinetic energy of the impacting drop to its surface energy or to the
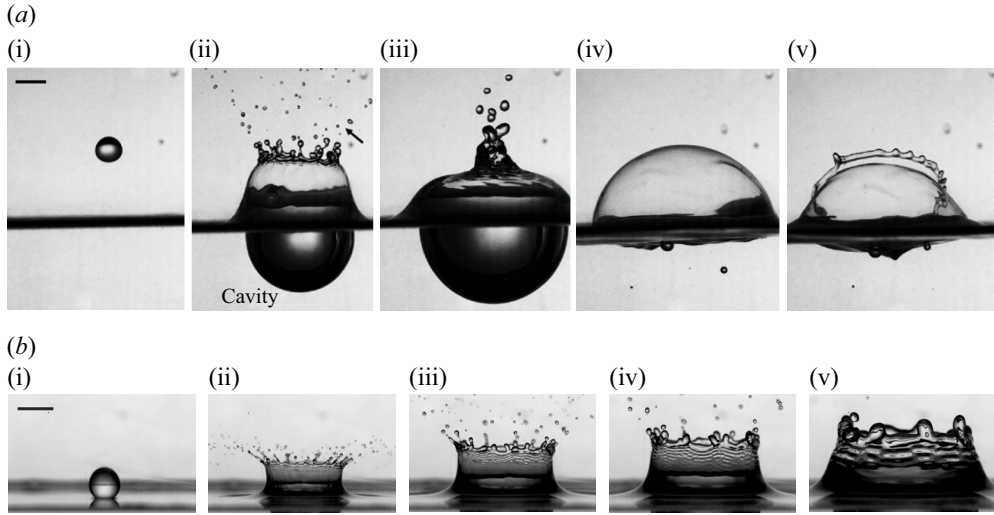
Figure 2. (*a*) Image sequence for (i) descending drop, (ii) bending crown, (iii) canopy development, (iv) bubble formation and (v) bubble burst during a drop–pool impact. These correspond to dimensionless time $tu_0/d_0 =$ 8.4, 16.8, 151.5, 185.1 in (ii)–(v) respectively. The impact Weber number is $We = 1700$ here. In (*a* ii), the arrow points to secondary droplets ejected from the splash canopy, typically formed at late time, when it forms. (*b*) Image sequence for the typical rise of an approximately cylindrical splash crown, up to maximum height, obtained for $We = 990$ and (i)–(v) $tu_0/d_0 = 0, 2, 4, 6, 14$. A scale bar of 5 mm is given for each sequence in (*a* i,*b* i).

potential gravitational energy, respectively. They are defined as

$$We = \frac{\rho u_0^2 d_0}{\sigma}, \quad Fr = \frac{u_0^2}{gd_0}, \quad (1.1a,b)$$

with ρ the density and σ the surface tension of the liquid. An extensive survey of different impact outcomes as a function of We and Fr is discussed in Murphy *et al.* (2015).

Most of the focus has been on drop impacts on thin liquid layers in which the layer thickness H is smaller than the impacting drop diameter d_0, i.e. $H \ll d_0$ (Rein 1993; Weiss & Yarin 1999; Wang & Chen 2000; Roisman & Tropea 2002; Josserand & Zaleski 2003; Cossali *et al.* 2004; Josserand, Ray & Zaleski 2016). A comprehensive survey of published experimental and numerical results obtained for thin films is reviewed by Liang & Mudawar (2016). In contrast, less attention has been paid to impacts on deep liquid layers (Engel 1966, 1967; Prosperetti & Oguz 1993; Agbaglah *et al.* 2015), where the resulting cavity–crown system shows distinctive characteristics. Here, a deep pool is defined to be one in which the air cavity at its maximum depth does not interact with the pool boundary. Such a pool has a typical thickness H much greater than the impacting drop diameter: $H \gg d_0$.

For impacts on deep pools, the cavity dynamics has received most attention, with an initial attempt to model its growth dynamics using a drop–cavity energy balance model Engel (1966, 1967). However, these results were limited given the incorrect potential flow field used therein (e.g. Lherm & Deguen 2023). Similarly, by assuming that entire drop initial energy is converted to cavity potential energy, Pumphrey & Elmore (1990) and Liow (2001) studied the maximum cavity depth D_m in terms of the drop diameter d_0 and its impacting velocity u_0. The accuracy and robustness of such energy analysis for a hemispherical cavity were further questioned by Bisighini *et al.* (2010), who instead

developed a descending sphere model based on potential flow and the Bernoulli equation. Lherm & Deguen (2023) extended this unsteady solution using a Legendre polynomial expansion. The cavity temporal evolution was also simulated numerically by Berberović *et al.* (2009), Morton, Rudman & Jong-Leng (2000), van Hinsberg *et al.* (2010), Ray, Biswas & Sharma (2015) and more recently Wang *et al.* (2023). Recently, the early time cavity dynamics immediately after the impact has garnered considerable interest for its key role in shaping subsequent events of the splash, including the crown formation and ejection of secondary droplets. During this initial contact, an ejecta consisting of the receiving pool extends horizontally below the impacting drop before a vertical sheet-like jet develops into a splash crown (Weiss & Yarin 1999; Thoroddsen 2002; Zhang *et al.* 2012). The interaction between these two jets and an entrapped air cushion leads to complex contact surface dynamics and a rich class of flow instabilities that are the subject of active investigations (Castrejón-Pita, Castrejón-Pita & Hutchings 2012; Thoraval *et al.* 2012; Agbaglah *et al.* 2015; Li *et al.* 2018). In this study, we focus on the late dynamics when a rising crown sheet has emerged from the receiving pool.

For drop impacts on thin, inviscid layers, Yarin & Weiss (1995) attributed the crown formation to the discontinuity in the velocity distribution at the interface using a quasi-one-dimensional (Q1D) approximation and derived an expression for the temporal evolution of the crown diameter ℓ, namely $\ell/d_0 \propto (tu_0/d_0)^{1/2}$. Roisman & Tropea (2002) extended the discontinuity theory of Yarin & Weiss (1995) to predict the crown motion and shape in two dimensions.

Cossali, Coghe & Marengo (1997) also analysed the crown diameter temporal evolution for impacts on thin films and found that the crown size grows as the square root of time, in agreement with the prediction of Yarin & Weiss (1995). These findings were verified numerically by Rieber & Frohn (1999). Several studies aimed to decipher the crown rim instability (Fullana & Zaleski 1999; Roisman *et al.* 2007; Krechetnikov & Homsy 2009; Roisman 2010; Zhang *et al.* 2010), with a particular interest, again, on impacts on thin films. In contrast to the dynamics on thin films, analytical expressions for the dynamics of the crown diameter and height for drop impacts on deep pools continue to be missing. Further, for deep pool impact, the complete sequence and coupling of the events from cavity to crown to secondary droplets remain poorly understood. For example, the crown sheet velocity and thickness profiles, which are essential descriptions of the crown evolution in both time and space, have not been reported, except estimates given by Cossali *et al.* (2004) and Aljedaani *et al.* (2018) in the thin-film regime. Although in principle the detailed crown dynamics could be examined using numerical simulations (e.g. Fujimoto *et al.* 2001; Agbaglah *et al.* 2015; Fudge, Cimpeanu & Castrejón-Pita 2021), the absence of a theoretical framework for crown modelling presents major challenges in predictions for the secondary droplets ejected from the rim of the crown (figure 1).

In this paper, we combine experiments and theory to examine the coupled cavity–crown system with a focus on the regime of crown splash (figure 1*a*). For $We \gtrsim 1600$, the crown bends inwards leading to the formation of a canopy (figure 2*a* iii) (Engel 1967; Murphy *et al.* 2015). The canopy can also lead to the formation of a bubble, that can produce microdroplets via the well-known film rupture mechanism, the size and speed of which depend on the thickness and composition of the film (Lhuissier & Villermaux 2012; Poulain, Villermaux & Bourouiba 2018) as illustrated in figure 2(*a* iv,v). Film bubble drops are distinct families of secondary droplets that can be enriched in contamination from the pool. These were studied elsewhere (Poulain *et al.* 2018; Poulain & Bourouiba 2018, 2019; Bourouiba 2021*a*) and are beyond the scope of this paper. As a result, here, we focus our attention on the range of *We* identified experimentally to ensure splash without canopy closure: $500 < We < 1600$ for water drops impacting deep-water pools.
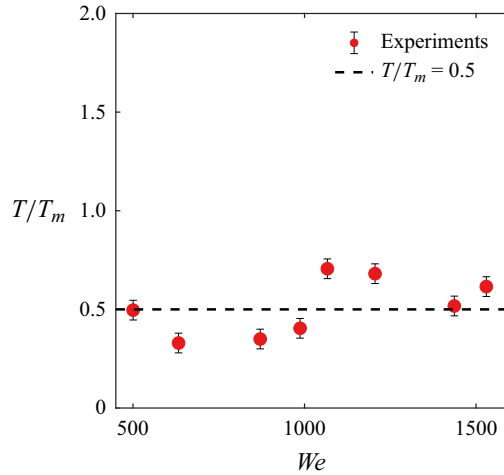
Figure 3. All of the secondary droplets are ejected from the crown rim by T_m, the time of maximum crown height. The figure shows the point in time in which about 95 % of the microdroplets detected from the crown have been emitted. This occurs around half the time of maximum crown height over the full range of *We* we consider. Here, t_m is the dimensional time at which the crown reaches its maximum height and $T_m = t_m\sqrt{\sigma/\rho d_0^3} \approx 1$ is the associated dimensionless time non-dimsionalized with the capillary time. An average of 10 experiments are shown per *We* here, again, focusing on a regime of crown splash free of canopy closure and where tracking of appearance of the droplets emitted by the crown is done regardless of their size.

Figure 2(*b*) and supplementary movie show a typical splash development in this regime where an approximately cylindrical crown arises, shedding droplets around the rim. It is interesting to note that for such a splash regime, most secondary droplets are ejected from the crown rim before the crown reaches its maximum height, an observation that remains valid over the full range of *We* in our range of interest (figure 3).

The rest of this paper is structured as follows. In § 2 we explain our measurement methods for the coupled cavity–crown system. We then analyse the cavity evolution in § 3 based on the model of Bisighini *et al.* (2010). We derive an asymptotic solution to the model that captures the experiments. We devote § 4 to examining the splash crown, modelled as a double-sided cylindrical sheet. Connection to the cavity expansion is first established empirically for the crown diameter. We subsequently invoke the thin-film approximation for the crown sheet, leading to conservation equations for a Q1D flow. We solve the corresponding initial-value problems asymptotically for the velocity field, the thickness profile and the height evolution of the crown sheet. Our analytical results are validated using experimental measurements. We discuss the conclusions in § 5.

2. Experiments and measurement methods

We release one water drop at a time from a range of heights on a liquid pool, made of the same fluid as that of the impacting drop. We consistently produce water drops of diameter $d_0 \approx 4$–4.7 mm as shown in figure 4(*a*) to impact a tank that ensures deep-pool conditions, with dimensions on all sides and in depth that are more than 10 times the diameter of the impacting drop. The effective diameter of the drop is measured from its area and used as the impacting drop diameter d_0 (Wang & Bourouiba 2023, 2018). We vary the imparted energy of impact by changing the drop release heights, with impact velocities measured to be up to $u_0 = 5$ m s^{-1} at the point of impact. These values are associated
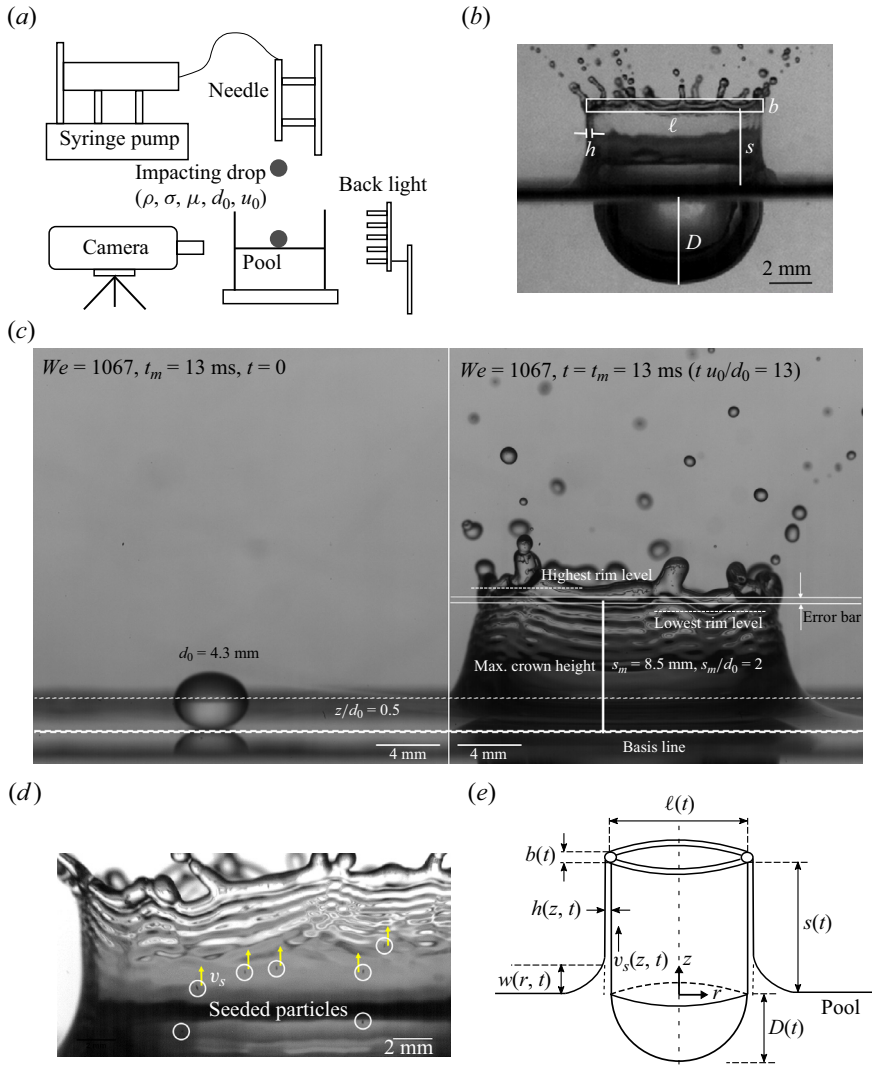
Figure 4. (*a*) A drop is released from heights varying from 2 to 5 mm. Backlighting with a diffuser is used to visualize the splash with a high-speed camera. (*b*) A typical cavity–crown image with key dimensions labelled is shown. The rectangle here encloses the corrugated rim without all the attached ligaments. The width b is the characteristic rim diameter. (*c*) Left: drop from the surface determined at point of impact using reflection on the interface. Right: the resulting crown at its maximum height. The crown height is defined between the unperturbed pool interface to the mean base rim level. Note the relatively higher curvature for heights below $z/d_0 = 0.5$, preventing measurements of particle velocity in and thickness of the sheet. This relatively higher curvature junction is also visible in figure 2(*b*). We also illustrate the uncertainty of the crown height introduced mostly by the error on detection of the base of the rim. Note that the error on the edge of rim detection is typically larger than the standard deviation of crown heights between repeat experiments. Meanwhile, the variability of rim level measured at different azimuthal angles is typically twice that of the crown height error shown here. (*d*) Particle tracking for the sheet velocity measurement. The particles used are of $\approx 50\,\mu$m with error on position of their centre no larger than 2–3 pixels, that is, at most 0.03 mm, which is smaller than their distance travelled over the sampling time we find sufficient to determine their speed in subsequent sections and figure 8, e.g. ≈ 0.5 mm. (*e*) Schematic of the modelled cavity–crown system formed upon drop impact on a liquid pool in axisymmetric cylindrical coordinates (r, z). The cavity depth $D(t)$, wave swell profile $w(r, t)$, crown sheet thickness $h(z, t)$, crown height $s(t)$, crown diameter $\ell(t)$, rim diameter $b(t)$ and crown sheet velocity $v_s(z, t)$ are shown.

Quantity of interest	u_0 (m s^{-1})	d_0 (mm)	We	Fr	Bo	Re $\times 10^4$	No. of exp.
Cavity depth, D	3–5	4–4.7	500–1600	195–630	2–3	1.2–2.3	40
Crown sheet velocity, v_s	3–5	4–4.7	500–1600	195–630	2–3	1.2–2.3	20
Crown sheet thickness, h	3.7–5	4.7	900–1600	290–540	3	1.7–2.3	20
Crown diameter, ℓ	3–5	4–4.7	500–1600	195–630	2–3	1.2–2.3	100
Crown height, s	3–5	4–4.7	500–1600	195–630	2–3	1.2–2.3	100

Table 1. Experimental conditions for water drop impacts on water pools when examining various quantities of interest (leftmost column). Deionized water was used for both the impacting drop and the pool fluid with density, kinematic viscosity and surface tension $\rho = 1 \times 10^3$ kg m^{-3}, $\mu = 1 \times 10^{-3}$ mPa s and $\sigma = 72 \times 10^{-3}$ mN m^{-1}, respectively. The values of the Weber number $We = \rho u_0^2 d_0/\sigma$, Froude number $Fr = u_0^2/g d_0$, Bond number $Bo = \rho g d_0^2/\sigma$, Reynolds number $Re = \rho u_0 d_0/\mu$ and the number of experiments performed are also provided.

with Weber numbers up to $We \approx 1600$. To minimize impact effects associated with the initial shape of an impinging drop, we chose the release heights so that at the impact time, $t = 0$, all drops share a similar aspect ratio caused by the capillarity-induced shape oscillations during free-fall. High-speed imaging is conducted using back-lighting along with a classical diffuser and at frame rates of 3200–5000 per second (fps) for the colour camera and 10 000–12 500 fps for the monochrome camera for most impacts, or higher if need be for the very early time dynamics, and up to 30 000 fps. The experimental set-up was designed to minimize vibration, and experiments were conducted in a laboratory with ambient temperature control. Lighting was designed, installed and used to minimize heating effect on the pool. A combination of imaging was done: some focusing on the crown above the interface pool; some focusing on the cavity below the interface pool; and some capturing both top and bottom dynamics across the interface. Measurements account for the presence of a meniscus with regard to crown height, crown thickness and velocity profile, as discussed in the relevant sections and figure captions. We only focus on the range of We identified experimentally to ensure splash without canopy closure: $500 < We < 1600$ for water drops impacting deep-water pools, as seen for example in the sequence of figure 2(*a*). The range of parameters and values used are given in table 1.

Table 1 also lists five key quantities that we consider for the cavity–crown system in a splash experiment, as illustrated in figure 4(*b*). These include the cavity depth D, the crown diameter ℓ, the axial flow velocity in the crown sheet v_s, the crown sheet thickness h and the crown height s. Specifically, D is measured between the undisturbed pool surface and the lowest cavity point; ℓ is the horizontal distance between the outer sheet boundary taken immediately below the lowest elevation of the rim. Note that s is the vertical distance between the unperturbed pool surface and the spatially averaged lower rim boundary along the azimuth, θ. We define crown height s based on such a mean value to remove fluctuations caused by any periodic rim instabilities (e.g. of the Rayleigh–Plateau type). Specifically, perturbations over the mean value s in the form of $\tilde{s}(\theta, t) = \sum_{n \neq 0} c_n(t) e^{in\theta} \in \mathbb{R}$ do not alter s for all permissible time-dependent complex amplitudes $c_n(t)$ and wave modes $n \in \mathbb{Z}$ due to the identity $\int_{-\pi}^{\pi} \tilde{s} \, d\theta = 0$. Averaging also mitigates random spatial inhomogeneities introduced in the initial impact dynamics. As a result, our measurement of s is expected to approximate an axisymmetric quantity well, offering robust characteristics of the splash across experiments repeated under the same conditions (including camera settings). Note that the modal amplitude c_n of the rim

instabilities is not the focus of this paper. For this reason, we also distinguish experimental uncertainty associated with s from the variability of the rim levels at different azimuthal locations. Typically, the former is mostly introduced by edge detection algorithms that determine the rim boundary in images captured under specific settings; whereas the latter is caused by rim instabilities and inhomogeneous impact, whose magnitude in our case is at most twice that of the error in s, as shown in figure 4(*c*). In comparison, the standard deviation of s measurements obtained between repeated experiments is consistently smaller than the s error associated with rim edge detection methods at all times. While length measurements of D, ℓ and s can be obtained using standard image processing techniques, measurements of v_s and h require dedicated treatments.

First, to determine the sheet velocity profile, in a separate set of experiments, we seed the impacting drop and the pool fluid with polyethylene microspheres of $\approx 50\,\mu$m in diameter and a density of 1 ± 0.05 g mL^{-1} at a concentration of about 0.2 g per 10 mL. These particles are used as flow tracers. Trajectories of the particles entering the crown sheet at varied times are captured (figure 4*d* and supplementary movie) for both the drop fluid and the pool fluid associated with a wide range of impacting Weber numbers ($500 < We < 1200$).

Next, to measure the sheet thickness profile, we use a light absorption method (Vernay, Ramos & Ligoure 2015; Wang & Bourouiba 2017; Si *et al.* 2024). We select the use of nigrosin which we have established, in prior work (Wang & Bourouiba 2017), to follow the Beer–Lambert law of absorption even with non-monochromatic white light:

$$h = \epsilon \ln\left(\frac{I_0}{I}\right), \tag{2.1}$$

where I_0 is the incident background light intensity and I is the transmitted light intensity after passage through a film of thickness h (e.g. Wang & Bourouiba 2017; Si *et al.* 2024). Here, $\epsilon = 1/(\gamma C) = 2220\,\mu$m with absorptivity $\gamma = 4.5 \times 10^{-3}$ L (g μm)$^{-1}$, given a nigrosin dye concentration of $C = 0.1$ g L^{-1} herein. Moreover, I is the measured intensity of transmitted light after passage through two films of thickness h, i.e. $2h$, rather than just one. Moreover, in the crown geometry considered here, we measure intensity only above the point of highest curvature marking the 'wave swell', typically above $z = 0.5$ as seen, for example, in figure 4(*c*).

3. Cavity dynamics

We begin our analysis with the evolution of the cavity below the liquid surface generated by the impacting drop. An axisymmetric cylindrical coordinate system (r, z) with origin located at the initial drop–pool contact point at time $t = 0$ is used to describe the cavity–crown structure (figure 4*d*). Based on Bisighini *et al.* (2010), we derive an explicit approximate expression for the cavity depth $D(t)$ in the large We and Fr limits that captures the experimental measurements well, up to maximum depth.

3.1. *Governing equations for the cavity*

Bisighini *et al.* (2010) model the cavity as an expanding sphere of radius $a(t)$ centred at $z = -z_c(t)$ along the axial direction. Assuming potential flow for the liquid surrounding the cavity and consequently balancing pressure along the crater boundary obtained from the linearized Bernoulli equation with surface tension, i.e. enforcing the Young–Laplace

equation near the cavity bottom $z = -D(t)$, one derives the following non-dimensional ordinary differential equations (ODEs) for the cavity:

$$\ddot{a} = -\frac{3\dot{a}^2}{2a} - \frac{2}{We\,a^2} - \frac{z_c}{Fr\,a} + \frac{7\dot{z}_c^2}{4a}, \tag{3.1a}$$

$$\ddot{z}_c = -\frac{3\dot{a}\dot{z}_c}{a} - \frac{9\dot{z}_c^2}{2a} - \frac{2}{Fr}, \tag{3.1b}$$

where the overdot denotes time derivatives, the Weber number We and Froude number Fr are defined in (1.1a,b) and we have chosen the reference length d_0 (impacting drop diameter), velocity u_0 (impacting velocity) and time d_0/u_0 to obtain dimensionless variables. We henceforth default to this inertial scaling in the rest of this study unless otherwise stated.

The initial condition associated with (3.1) must be specified at a non-zero time $t = t_0 \gtrsim 2$ to allow for sufficient time for the cavity formation caused by the initial drop penetration process (Fedorchenko & Wang 2004; Berberović *et al.* 2009; Wang *et al.* 2023). Detailed discussion for such early phase drop deformation is not the focus of this study. Instead, we close (3.1) with initial values measured experimentally at around $t_0 \approx 1.5$ when the cavity shape starts to take a spherical cap. Subsequently, the crater depth can be modelled using $D(t) = a(t) + z_c(t)$ for $t > t_0$.

3.2. *Asymptotic solutions*

One important solution to (3.1) in the $We \to \infty$ and $Fr \to \infty$ limits, with $\dot{z}(t_0) = z(t_0) = 0$, is given by

$$a(t) = A(t - t_s)^{2/5}, \quad z_c(t) = 0, \tag{3.2a,b}$$

where A and t_s are constants. This scaling law is well known; for example, Berberović *et al.* (2009) estimated that $A = (5/4)^{2/5}$, $t_s = 6/5$.

Next, we develop an asymptotic correction for z_c, noting that the coupling between a and z_c in (3.1a) is weak if the cavity's radial expansion dominates its axial translation, i.e. $|z_c/a| \ll 1$. In this case, (3.2a,b) also holds for moderate Fr and large We. Therefore, substituting (3.2a,b) into (3.1b) while considering $|\dot{z}_c/\dot{a}| \ll 1$ leads to

$$\ddot{z}_c + \frac{6\dot{z}_c}{5(t - t_s)} + \frac{2}{Fr} = 0, \tag{3.3}$$

which can be solved exactly to give

$$D(t) = a + z_c = A(t - t_s)^{2/5} + \frac{-5t^2 + 10t_s t}{11\,Fr} + \frac{c_1}{(t - t_s)^{1/5}} + c_2, \tag{3.4}$$

where c_1 and c_2 are constants determined by initial values. Equation (3.4), parametrized by Fr, offers an explicit approximate solution to (3.1) in the strict limit of $We \to \infty$.

Compared with (3.2a,b), the correction offered by finite $Fr > 0$ in (3.4) alters the monotonic behaviour of the original limit and introduces a global maximum for D as t increases. Physically, this is consistent with the fact that the cavity depth must retract after its initially growth and penetration into the pool due to gravitational effects. The kinematic reason for such retraction is that the centre of the air cavity $-z_c$ given by (3.3) with $Fr > 0$ rises over time, i.e. $z_c < 0$ and $\dot{z}_c < 0$. Originally, Fr enters (3.1b) because gravitational potential for the liquid flow field around the cavity is incorporated in

the dynamic Bernoulli equation. Therefore it is primarily the gravitational pull on the displaced liquid that stops the air cavity from penetrating the pool indefinitely, rather than surface tension. A direct comparison between these two restoring forces for cavity retraction is given in § 3.3.1. In contrast, we also show later in § 4.4 that the leading-order mechanism that modulates the growth of an initially rising crown is surface tension rather than gravity.

3.3. *Experimental and numerical results*

We now can compare the cavity depth measurements with the models of (3.1), (3.2*a*,*b*) and (3.4). All experimental data obtained at early times are aggregated and follow (3.2*a*,*b*). However, given the open questions regarding the very initial details of the impact, the constants are impossible to predict at this time. The constants are found to be $A = 1$ and $t_s = 1.4$ using a least-squares method, and close to the values of Berberović *et al.* (2009). Accordingly, $z(t_0) = \dot{z}(t_0) = 0$ and $a(t_0)$, $\dot{a}(t_0)$ are evaluated using (3.2*a*,*b*) as initial conditions. Solutions to (3.1) are calculated numerically using a fourth-order Runge–Kutta scheme.

Figure 5(*a*) shows comparisons of $D(t)$ for experiments and theory for three sets of increasing *We* and *Fr*. In all cases, the numerical solution to (3.1) is in agreement with the measurements over time, well beyond the instant of maximum cavity depth. This is not surprising as similar verification for the model of Bisighini *et al.* (2010) was also provided in Lherm & Deguen (2023) and Wang *et al.* (2023) with different initial conditions. In addition, we show the performance of the two asymptotic solutions (3.2*a*,*b*) and (3.4) for each experiment: the improvement made by the *Fr*-dependent approximation (3.4) over the limiting power law (3.2*a*,*b*) is clear. Specifically, (3.2*a*,*b*) as a monotonically increasing function can only capture measurements of cavity dynamics at early times, whereas (3.4) provides a theoretical peak enabled by gravitational effects of finite *Fr* that overall corrects (3.2*a*,*b*) close to the observed maximum depths.

3.3.1. *Universal underlying dynamics on the capillary time scale*

Now we consider a different asymptotic regime for (3.1*a*) where the $Fr \to \infty$ limit is taken for large but finite *We*. By expanding (3.1*a*) in power series of $We^{-1} \ll 1$, we explicitly derive in Appendix A.1 the leading-order solution and its next-order correction as follows:

$$a(t) = A(t - t_s)^{2/5} + \frac{1}{We}\left[-\frac{25(t - t_s)^{6/5}}{18A^2} + A_1(t - t_s)^{2/5}\right] + O\left(\frac{1}{We^2}\right), \quad (3.5a)$$

$$\frac{D(\tau)}{We^{1/5}} \sim \frac{\tau^{2/5}}{6^{1/5}} - \frac{25\tau^{6/5}}{18 \times 6^{3/5}}\frac{1}{We^{2/5}}, \quad (3.5b)$$

where in (3.5*b*) we have used the capillary time τ (with its dimensional reference T_{cap}) given by

$$\tau = t\sqrt{\frac{6}{We}}, \quad T_{cap} = \sqrt{\frac{\rho d_0^3}{6\sigma}}, \quad (3.6a,b)$$

with t the time defined earlier as non-dimensional time with respect to impact time, i.e. $t =$ dimensional time/(d_0/u_0). As $We \to \infty$, (3.5*b*) thus suggests that D scales with $We^{-1/5}$ at leading order while a capillary restoring term decays as $We^{-2/5}$. Figure 5(*c*) shows the rescaled $D(\tau)/We^{1/5}$ as a function of τ. Our experimental data for D of specific ranges of *We* and *Fr* collapse well under such capillary normalization. However, the corresponding
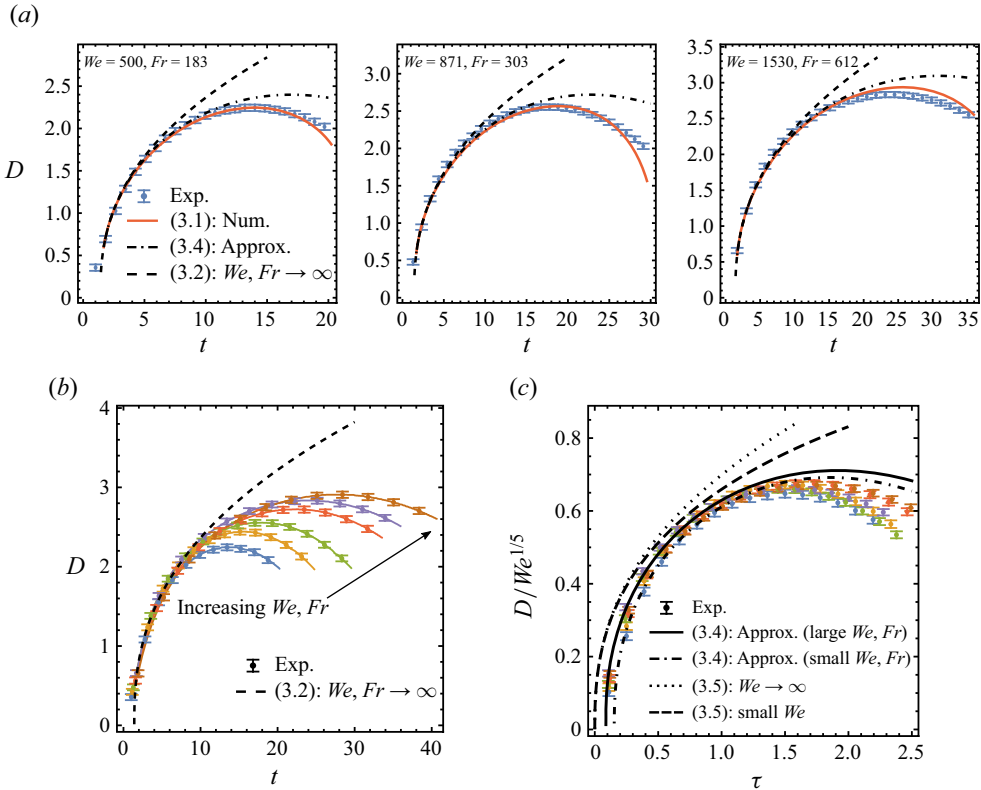
(*a*)

(*b*)

(*c*)

Figure 5. Time evolution of cavity depth D. In the three panels of (*a*), experiments are compared to theory in the limit of $We, Fr \rightarrow \infty$ (see (3.2*a,b*)) and for the approximation $|z_c/a| \ll 1$ and $|\dot{z}_c/\dot{a}| \ll 1$ for increasing We and Fr. In each case, the solid line shows numerical solution to (3.1), the dashed line gives the limiting law of (3.2*a,b*) and the dash-dotted line plots the approximation of (3.4). (*b*) Plot of $D(t)$ over inertial time t shown for $(We, Fr) = (500, 183), (633, 232), (871, 303), (1067, 420), (1434, 509), (1530, 612)$. The dashed limit (3.2*a,b*) captures all $D(t)$ data at early times. (*c*) Rescaled $We^{-1/5}D$ as a function of capillary time τ (see (3.6*a,b*)) that collapses the same measurements given in (*b*). Here the dotted and dashed lines respectively show the rescaled (3.5*b*) for $We = \infty$ and $We = 500$, while the solid and dot-dashed lines respectively show (3.4) evaluated using $(We, Fr) = (500, 183)$ and $(1434, 509)$. The error bars shown capture the error of detection of the edge of the cavity.

capillarity-dominant model (3.5*b*) does not capture the collapsed data in this case, whereas the gravity-dominant model (3.4) shows better agreement.

Note the distinction with the effects of varying We and Fr on the cavity depth evolution examined next in figure 5(*b,c*). Under the default inertial scaling, a series of $D(t)$ measurements by increasing $We = 500, Fr = 183$ to $We = 1530, Fr = 612$ are also given in figure 5(*b*). We find that all experiments share the same initial rise that follows the large We, Fr law of (3.2*a,b*), which justifies our estimation of $A = 1$ and $t_s = 1.4$ discussed previously. By increasing We and Fr, larger maxima of $D(t_m)$ are observed at larger times $t = t_m$. In addition, figure 5(*c*) shows a direct comparison between cavity retraction due to gravity and surface tension, using (3.4) and (3.5*b*), respectively. Even at the lowest experimental value $We = 500$, the retraction correction of $O(We^{-2/5})$ in (3.5*b*) does not increase quickly enough to take over the leading-order cavity growth $D \propto \tau^{2/5}$, whereas (3.4) of finite Fr successively generates maximum cavity depths near the measured peaks. Therefore, we conclude that gravity is the dominant restoring force for the cavity.

4. Crown sheet dynamics and coupling with cavity

In this section we develop a simplified theory for the development of the crown sheet as a result of drop impact. We take the crown geometry to be approximated as a double-wall cylinder of spatially uniform diameter $\ell(t)$, axially varying thickness $h(z, t) \ll \ell$ and height $s(t)$, as illustrated in figure 4(*e*). This simplified geometry does not accommodate a sheet of oblique angles nor bending near the wave swell and the rim. More elaborate crown sheet geometries have been studied for drop impact against thin films (Roisman & Tropea 2002; Fedorchenko & Wang 2004), but it was established that films of larger thickness comparable with the drop size ($H/d_0 \sim 1$) always produce a vertical crown perpendicular to the liquid layer (Wang & Chen 2000; Fedorchenko & Wang 2004). This is consistent with our impact experiments on a deep pool ($H/d_0 \gg 1$) where a vertically rising crown sheet can be reasonably identified as the top rim separates away from the bottom wave swell. In the experiments, both $\ell(t)$ and $s(t)$ are measured immediately below the crown rim. Due to mass transfer enabled by the outward velocity within the thin sheet, $v_s|_{z=s}$, the rim destabilizes into corrugations, then ligaments that ultimately fragment into secondary droplets (figure 1). Here, we idealize the rim as a torus of ring diameter $b(t)$, neglecting its local azimuthal topological variation induced by instability and fragmentation. Given the geometry involved, we also invoke the thin-film approximation. Despite these geometric simplifications, next we derive analytical expressions for v_s, h and s that are in good agreement with our measurements.

4.1. *Crown diameter from cavity dynamics*

Following Yarin & Weiss (1995) who related the crown expansion to the propagating cavity in a thin film as a kinematic discontinuity, the diameter of the crown sheet above a liquid layer has been investigated extensively, as reviewed by Liang & Mudawar (2016). In those studies, a power law of the form $\ell(t) = \alpha(t + c)^p$, independent of *We* and *Fr*, is widely reported, with the exponent in the range $0.4 < p < 0.5$. On the other hand, results obtained for a crown sheet generated in a deep pool are scarce. Notably, Roisman, van Hinsberg & Tropea (2008) extended the kinematic discontinuity theory of Yarin & Weiss (1995) and derived an expression for the cavity evolution, and therefore the crown diameter measured at its base $\ell = \ell(t; We, Fr, H)$, incorporating a finite liquid layer thickness H (dimensionless). However, their expression cannot be generalized to the deep-pool limit as it diverges for $H \to \infty$ at any finite *We* and *Fr*. Instead, its $We \to \infty$, $Fr \to \infty$ limit exists for any given H, recovering the well-known result of Yarin & Weiss (1995), i.e. $\ell \propto \sqrt{t + c}$.

Similar to the geometrical argument made by the kinematic discontinuity theory, here the crown sheet expansion above a deep pool must also be related to that of the underneath cavity. Therefore we propose a model such that after the initial sheet formation when $t > t_0 \approx 1$, the sheet diameter ℓ grows in accordance with the asymptotic cavity depth D. Specifically, using the $We \to \infty$ limit of (3.5*b*), we propose

$$\ell(t) = \alpha D(t + c) \sim \alpha(t + c)^{2/5}, \tag{4.1}$$

where the proportional constant α is independent of time t but could depend on *We* and *Fr*, and the time shift c accounts for the observation that the crown sheet develops measurable diameters before the cavity forms.

Indeed, (4.1) captures the experimental data well (figure 6). The best-fit α and c values are of order unity and vary little from a set of *We*, *Fr* to another. Moreover, in figure 6(*b*) we compare the long-time behaviour of (4.1), i.e. $\ell \propto t^{2/5}$, and the thin-film result of Yarin
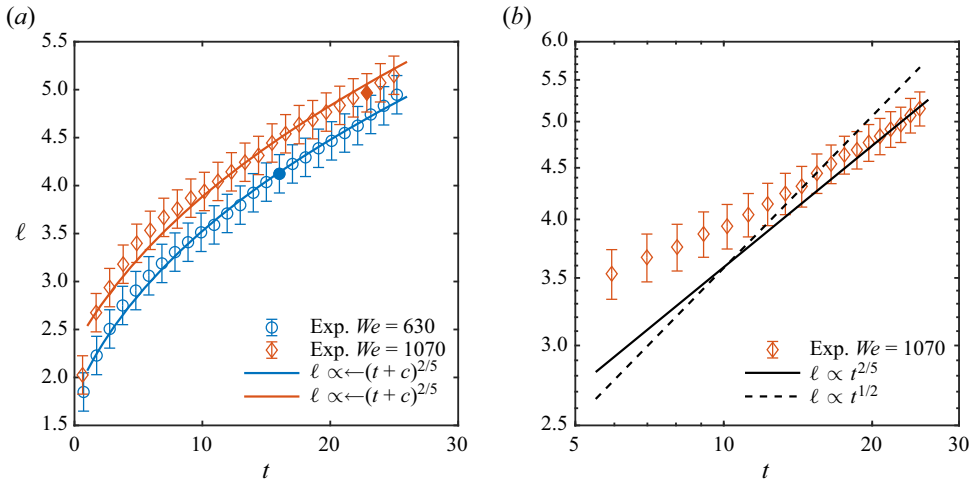
Figure 6. Time evolution of the crown diameter $\ell(t)$. (*a*) Experiments are compared with the model of (4.1), with fitted $\alpha = 1.3$, $c = 2.2$ and $\alpha = 1.4$, $c = 3.7$ for $We = 630$ and 1070, respectively. The two filled data points mark the time when the maximum cavity size is reached in each corresponding experiment. (*b*) Comparison between the large-time asymptotic theory given by (4.1) where $\ell \propto t^{2/5}$ and the thin-film limit of Yarin & Weiss (1995) where $\ell \propto t^{1/2}$ against the measurements of $We = 1070$. We establish that (4.1) captures the ℓ data well with the long-time growth scaling closer to $t^{2/5}$. Note that all proportional constants are $O(1)$ and in fact their specific value is not needed to model the axial crown development, as we see in § 4.3.1. The error bars capture the uncertainty of detecting the outer sheet boundary in the radial direction, at rim base evaluation.

& Weiss (1995), i.e. $\ell \propto t^{1/2}$, against measurements obtained for the larger $We = 1070$ on a logarithmic scale. As t increases, the data follow more closely the asymptotic growth given by $t^{2/5}$ compared with the thin-film limit $t^{1/2}$. Capturing the correct scaling law for the crown diameter is particularly important for our subsequent analysis because we show next in §§ 4.3 and 4.4 that the specific best-fit value of the proportional constant α is, in fact, not needed for the derivation of the crown thickness and height.

Notably, unlike the peaking behaviour observed for the $D(t)$ measurements shown in figure 5, here we find that the $\ell(t)$ data given in figure 6 are close to monotonic, captured by a power law $t^{2/5}$ that is derived for $D(t)$ in the strict limit of $We, Fr \to \infty$. The fact that the growth of $\ell(t)$ under finite We and Fr beyond the time of maximum cavity depth (labelled in figure 6a) still yields good prediction for the crown requires further mechanistic investigation left for future work. Informed by the cavity dynamics and its coupling with the crown, we can now focus on solving for the crown sheet dynamics, including its thickness in § 4.3 and height in § 4.4.

4.2. *Unsteady crown sheet spatio-temporal velocity profile*

4.2.1. *Quasi-one-dimensional flow*

Next we examine the flow velocity field $\boldsymbol{u}$ in the crown sheet using thin-film lubrication theory (Batchelor 1967). Generally, the sheet flow is axisymmetric, i.e. $\boldsymbol{u} = u_s \hat{\boldsymbol{r}} + v_s \hat{\boldsymbol{z}}$ where $\hat{\boldsymbol{r}}$ and $\hat{\boldsymbol{z}}$ are, respectively, the radial and axial unit vectors. Here, $\boldsymbol{u}$ is governed by

the incompressible Navier–Stokes equations:

$$\begin{cases} \nabla \cdot \boldsymbol{u} = 0, & (4.2a) \\[2mm] \dfrac{\partial \boldsymbol{u}}{\partial t} + \boldsymbol{u} \cdot \nabla \boldsymbol{u} = -\nabla p + \dfrac{1}{Re}\nabla^2 \boldsymbol{u} - \dfrac{\hat{\boldsymbol{z}}}{Fr}, & (4.2b) \end{cases}$$

where p is pressure and $Re \equiv \rho u_0 d_0 / \mu$ is the Reynolds number. Before proceeding, we reiterate the modelling assumption that the crown sheet up to the rim, within $0 < z < s(t)$, approximates a vertical wall of inner diameter $\ell(t) - h(z,t)$ and outer diameter $\ell(t) + h(z,t)$, where the diameter of the central ring $\ell(t)$ is axially uniform. Note that although in experiments ℓ is measured as the sheet's outer diameter rather than the central ring diameter, differences between these two become negligible following the thin-sheet assumption, i.e. $h/\ell \ll 1$, $h/s \ll 1$. As illustrated in figure 4(*e*), the crown sheet domain is double-cylindrical as follows:

$$\mathcal{D}(t) = \left\{ (r,z) : 0 < \left| r - \frac{\ell(t)}{2} \right| < \frac{h(z,t)}{2},\ 0 < z < s(t) \right\}. \tag{4.3}$$

Therefore applying the lubrication approximation to (4.2*a*) and radially expanding the flow variables leads to the Q1D flow approximation:

$$v_s = v_s(z,t), \quad u_s = u_s(z,r,t) = \frac{\ell^2 - 4r^2}{8r}\frac{\partial v_s}{\partial z} \ll v_s \tag{4.4a,b}$$

that respects the continuity equation (4.2*a*) and the symmetry condition $u_s(z,\ell/2,t) = 0$. A formal derivation of (4.4*a,b*) is given in Appendix A.2.

The dynamic stress condition for the free surface of $\mathcal{D}$, i.e. the Young–Laplace equation, implies that $p \sim \kappa/We$, where $\kappa(z,t)$ is the surface curvature evaluated at $|r - \ell/2| = h/2$. In the limit of $Re \to \infty$, $Fr \to \infty$ and $We \to \infty$, (4.2*b*) thus simplifies to the inviscid Burger equation:

$$\frac{\partial v_s}{\partial t} + v_s \frac{\partial v_s}{\partial z} = 0, \text{ or equivalently, } \frac{\mathrm{d} v_s}{\mathrm{d} t} = 0 \text{ along the parcel's trajectory.} \tag{4.5}$$

For closure, we also prescribe a linear initial profile, $v_s(z,t_0) \propto z$, at some initial time $t_0 > 0$ shortly after the sheet forms such that the initial sheet height is small, i.e. $z < s(t_0) \ll 1$, and therefore a linear profile is valid as a Taylor series expanded around $z = 0$. This assumption, including the boundary value $v_s(0,t) = 0$, is further verified by direct measurement of v_s in § 4.2.3. As a result, using method-of-characteristics, (4.5) is uniquely solved by

$$v_s = \frac{z}{t - \delta}, \tag{4.6}$$

where $0 < \delta \ll 1$ is the offset time required for the onset of sheet formation after drop impact, with δ of the order of a fraction of the inertial reference time d_0/u_0 (0.7–1.4 ms). A similar time scale for such offset was discussed for drop impacts on solid surfaces (Wang & Bourouiba 2017). The physical origin for δ is discussed in more detail next.

4.2.2. *Sheet formation offset*

When the drop impacts the liquid substrate, the impact initially imparts a downward velocity to the fluid parcels in immediate contact with the liquid pool (figure 7*a*) and
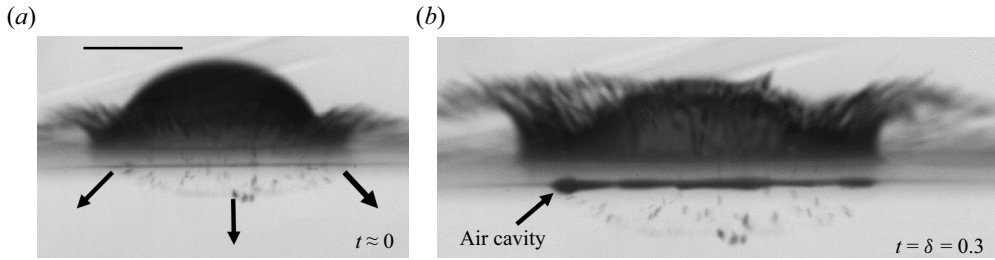
Figure 7. (*a*) Dynamics in the pool fluid at the instant when the drop fluid seeded with polyethylene microspheres impacts the pool. The impact imparts a downward momentum to the particles in the drop. Scale bar: 2 mm. (*b*) An air cavity forms, and is seen below the liquid surface at $t = \delta = 0.3$. The particles in the drop continue moving downward owing to their high initial momentum. In this experiment, $We = 900$.

the cavity develops. This allows the drop fluid to spread onto the developing cavity floor. The accumulated drop fluid is stretched in the radial direction owing to the cavity's radial expansion. The discontinuity in the velocity distribution at the interface causes the formation of an upward-moving lamella that eventually forms the crown sheet (Yarin & Weiss 1995; Roisman & Tropea 2002). This upward motion stretches the drop fluid in the vertical direction, leading to the formation of the developing crown sheet. Hence, owing to the initial phase of lubrication with air cushion and establishment of the ejecta sheet and crown, it takes time for the sheet to appear. This time is of the order of the time taken for the air cavity to form below the substrate fluid. For $We = 900$, we first observe an air cavity appearing below the receiving liquid surface around $t = \delta \approx 0.3$, as shown in figure 7(*b*). Note that a similar time scale of $O(0.1)$ for the initial stages of sheet development can be seen in the experiments of Agbaglah *et al.* (2015) and numerical simulations of Josserand *et al.* (2016). In sum, the offset δ of the velocity profile in (4.6) accounts for the very initial time needed for sheet formation.

4.2.3. *Experimental validation*

Now we validate our solution for $v_s(z, t)$ given by (4.6) against direct experimental measurements introduced in § 2. Figure 8(*a*) first shows the trajectories of particles that were initially seeded in the impacting drop or the substrate pool. In both cases, all selected particles exhibit linear motion of constant speed for $500 < We < 1200$ considered, in agreement with the Lagrangian interpretation of (4.5), i.e. $\mathrm{d}v_s/\mathrm{d}t = 0$ where $\mathrm{d}/\mathrm{d}t$ denotes material derivative.

Further, figure 8(*b*) compares directly the complete integral solution (4.6) with the v_s measurements obtained from experimental particle trajectories. For both cases of seeded impacting drop or pool fluid tracking, $v_s(z, t)$ is obtained after averaging six experiments per *We*. The averaged data are captured very well with the theoretical expression with $\delta = 0.3$. The observation that measurements taken near $z = 0$ approach $v_s = 0$ also justifies our choice of the initial linear velocity profile, $v_s(z, t_0) \propto z$ for some $t_0 > \delta$, required to derive (4.6).

4.3. *Crown sheet thickness profile*

4.3.1. *Analytic thin-film model*

Now we turn our attention to the thickness profile $h(z, t)$ of the crown sheet. To derive its governing equations, we utilize the following integral form of the continuity equation
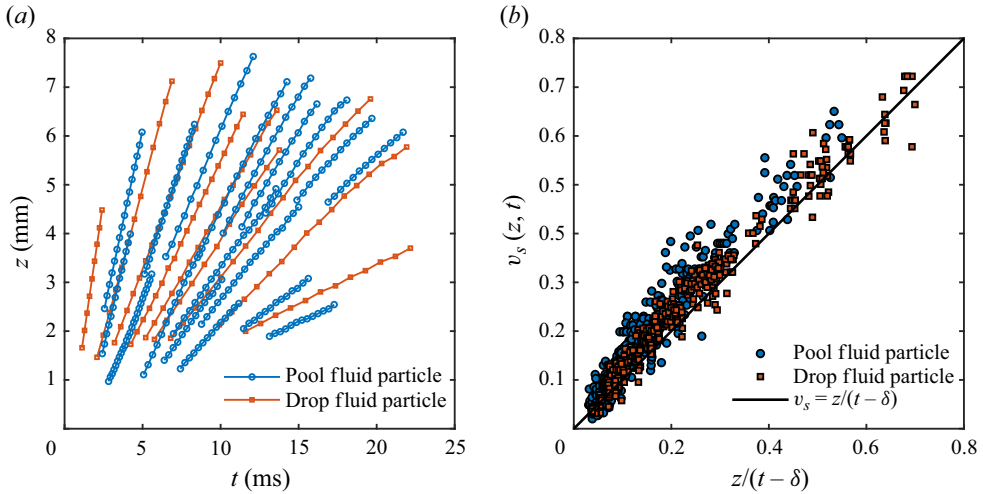
Figure 8. (*a*) Trajectories of particles in the crown sheet that were initially seeded in the impacting drop and the substrate pool. A subset of results for $We = 900$ is displayed for visual clarity. The same pattern is found for all We used, namely all particles show linear trajectories of constant velocity. (*b*) Comparison of the analytic solution (4.6), with $\delta = 0.3$, against the Eulerian sheet flow velocity v_s obtained from the particles in a range of experiments with $500 < We < 1200$. A good agreement between the theory and the experiments is observed.

(4.2*a*) and the simplified momentum equation (4.5):

$$I_\chi \equiv \frac{\mathrm{d}}{\mathrm{d}t} \int_\Omega \chi \, \mathrm{d}V + \oint_{\partial\Omega} \chi (\boldsymbol{u} - \boldsymbol{u}_b) \cdot \boldsymbol{n} \, \mathrm{d}A = 0, \qquad (4.7)$$

where $\chi = 1$ and $\chi = v_s$ are used for mass and momentum conservation, respectively, over a subdomain $\Omega \subset \mathcal{D}$. Here $\boldsymbol{u}_b$ defines the boundary velocity of $\partial\Omega$, up to an arbitrary tangential component, and $\boldsymbol{n}$ is the outward unit normal vector. We make the thin-film approximation as in § 4.2.1 and consider a differential volume $\Omega = \mathcal{D}(t) \cap (z, z + \mathrm{d}z)$, where the volume element reads $\mathrm{d}V(z, t) = A(z, t) \, \mathrm{d}z = \pi\ell(t)h(z, t) \, \mathrm{d}z$. As such, the boundary integral in (4.7) can be evaluated using (4.4*a,b*), the Taylor expansion $v_s(z, t) \sim v_s + \partial v_s/\partial z \, \mathrm{d}z$ and the kinematic condition for the liquid–air interface, which reads

$$(\boldsymbol{u} - \boldsymbol{u}_b) \cdot \boldsymbol{n} = 0. \qquad (4.8)$$

Therefore enforcing $\mathrm{d}I_\chi/\mathrm{d}z = 0$ as a result of (4.7) leads to governing equations for h that read

$$\frac{\partial}{\partial t} [h(z, t)\ell(t)] + \frac{\partial}{\partial z} [v_s(z, t)h(z, t)\ell(t)] = 0, \qquad (4.9a)$$

$$\frac{\partial}{\partial t} [v_s(z, t)h(z, t)\ell(t)] + \frac{\partial}{\partial z} \left[v_s(z, t)^2 h(z, t)\ell(t) \right] = 0. \qquad (4.9b)$$

We can derive the analytic solution, with substitution of (4.1) and (4.6) in the limits $t \gg c$ and $t \gg \delta$ into (4.9), giving

$$\frac{\partial h}{\partial t} + \frac{z}{t} \frac{\partial h}{\partial z} + \frac{7h}{5t} = 0, \qquad (4.10a)$$

$$\frac{\partial h}{\partial t} - \frac{z}{t} \frac{\partial h}{\partial z} - \frac{13h}{5t} = 0, \qquad (4.10b)$$

which can be integrated directly as

$$h(z, t) = \frac{\beta t^{3/5}}{z^2}, \tag{4.11}$$

where β is a constant to be determined from initial conditions. Note that because (4.9) is homogeneous and linear in ℓ, the proportionality factor α that would appear in (4.1) for the crown diameter, and which was found to be $O(1)$ for all *We*, does not affect the crown thickness profile.

Notably, our theoretical profile (4.11) implies that the crown sheet thickness increases over time at any given height in its domain. This quality agrees with the estimated sheet thickness measurements of Cossali *et al.* (2004) in the thin-film regime, but contrasts the finding of Aljedaani *et al.* (2018) where the crown wall rising from a thin film of lower viscosity stretches and thins quickly over time.

4.3.2. *Experimental validation*

Here we present the light absorption measurements of thickness h discussed in § 2 and make comparison with the similarity solution (4.11). First, for two different *We*, figure 9(*a,b*) gives h profiles as a continuous function of z at an increasing sequence of times. We clearly observe sheet thinning (decrease of h) in the axial direction at any given time and local sheet expansion (increase of h) as time increases. The behaviour of h associated with different *We* is qualitatively similar. Indeed, figure 9(*c*) shows a three-dimensional scatter of h measurements in the (z, t) space, where results from four different *We* show little variation as the data appear to lie on a common surface. Finally, figure 9(*d*) shows that the similarity profile (4.11) collapses all experimental data from figure 9(*c*) very well, with $\beta \approx 0.044$. We verify such a β value alternatively using initial values in the next section. Our analytical model shows larger discrepancy against initial measurements taken at small $t = t_0 = 1$. This deterioration is likely affected by the accuracy of the asymptotic crown size, $\ell \propto t^2/5$, enabled by the assumption $t \gg c$ in (4.1) that is necessary in the derivation of (4.11).

4.4. *Crown height evolution*

Having developed accurate models for the crown diameter ℓ, axial velocity v_s, and sheet thickness h as key components, we finally formulate in this section an ODE system for the crown height evolution $s(t)$. The initial-value problem is solved both numerically and asymptotically, leading to the discovery of $We^{5/7}$ scaling for the crown rise that captures the experiments well.

4.4.1. *Governing equations*

As illustrated in figure 4(*d*), in our approximation of the crown's axial rise, we choose a control volume around an idealized toroidal rim and neglect the mass and momentum flux loss due to secondary droplet ejection for now. Based on the same principle of (4.7), the mass and momentum conservation for the rim read here as

$$\frac{\pi}{4} \frac{\partial}{\partial t} \left[\ell(t) b(t)^2 \right] = [v_s(s, t) - \dot{s}(t)] \, \ell(t) h(s, t), \tag{4.12a}$$

$$\frac{\pi}{4} \frac{\partial}{\partial t} \left[\ell(t) b(t)^2 \dot{s}(t) \right] = -\frac{2\ell(t)}{We} - \frac{\pi \ell(t) b(t)^2}{4Fr} + \ell(t) h(s, t) \left[v_s(s, t) - \dot{s}(t) \right] v_s(s, t), \tag{4.12b}$$
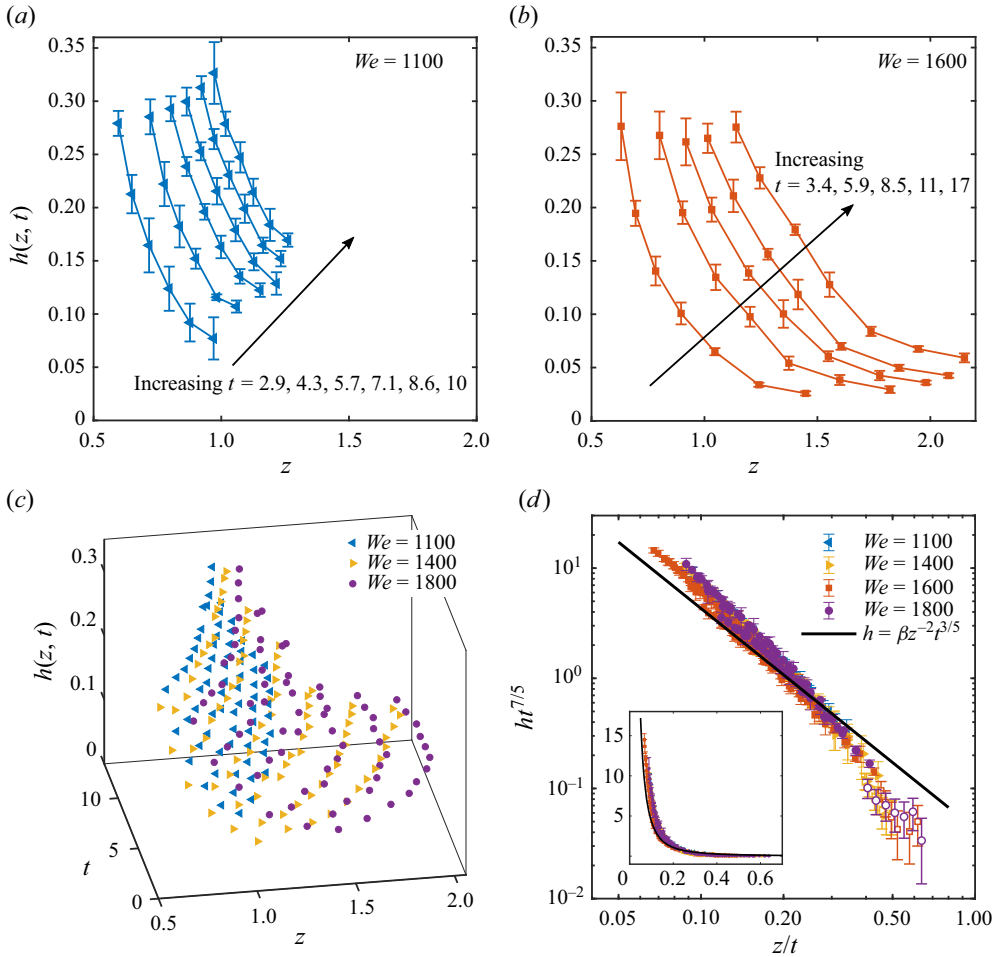
Figure 9. Evolution of the crown sheet thickness profile $h(z, t)$. We show the axial distribution of h at various times for (*a*) $We = 1100$ and (*b*) $We = 1600$. (*c*) A three-dimensional scatter of $h(z, t)$ for $1100 < We < 1800$, where variations due to different We are found to be small. (*d*) Direct comparison of all measurements and the similarity solution (4.11). The data collapse and agree with the theory very well. Largest relative deviations are found among initial data taken at $t = t_0 = 1$, marked by open symbols. The inset gives the same plot using linear scales, where the absolute error made by the theory remains small. Note that the measurements of thickness start at $z = 0.5$ to ensure that the region of most extreme curvature due to the wave swell is not included (recall the region of high curvature at the wave swell boundary seen in figure 4).

where $b(t)$ is the ring diameter. Importantly, we formally incorporate surface tension and gravity in the momentum equation (4.12*b*) while neglecting viscous stresses in the $Re \rightarrow \infty$ limit informed by the Re values given in table 1. The inviscid simplification is supported by Oguz & Prosperetti (1990), Trujillo & Lee (2001) and Roisman & Tropea (2002) who found that for high-velocity impacts on thin films, viscous effects on the dynamics of crown formation are small. As a result, the ODE system (4.12), parametrized by We and Fr, can be solved using numerical integration, provided with suitable initial values discussed next. We note again that (4.12) is linear in ℓ, rendering the equations independent of α in (4.1).
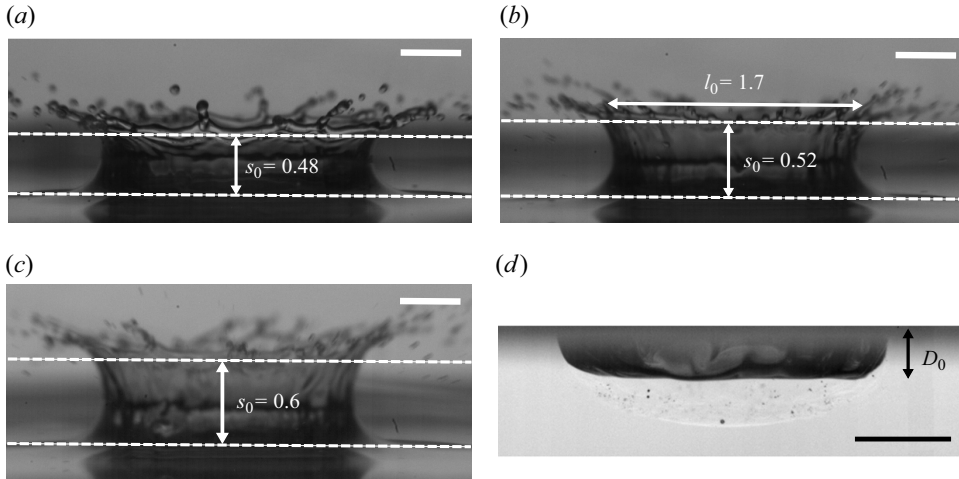
Figure 10. (*a–c*) Initial crown shapes taken at $t = t_0 = 1 \pm 0.03$ for increasing *We*: (*a*) $We = 500$, (*b*) $We = 990$ and (*c*) $We = 1440$. Crown diameter ℓ_0 and height s_0 are labelled. (*d*) Initial cavity of a cylindrical shape at $t = t_0$ for $We = 1070$, highlighting depth $D_0 = 0.23$. Scale bar: 2 mm for all panels.

4.4.2. *Initial conditions*

Considering the delay of crown sheet formation caused by early drop impact, as discussed in § 4.2.2, we select initial values for (4.12) at $t = t_0 = 1$ from experimental measurements when the crown structure has reasonably emerged. Figure 10(*a–c*) shows snapshots of the crown at $t = t_0$ for increasing *We*. It is generally observed that the initial crown height s_0 slowly increases with *We*. To simplify, we choose an averaged approximation of $s_0 = s(t_0) \approx 0.5$ and $\ell_0 = \ell(t_0) \approx 1.7$ next, citing an overestimation (or underestimation) of size of the order of 10 % relative to the measurements obtained at low (or high) *We* values. Further, we estimate that the initial axial growth rate is approximately $\dot{s}_0 = \dot{s}(t_0) \approx s_0/t_0$. Also, at this time the rim thickness is estimated in experiments to be $b(t_0) \sim O(0.01)$, and therefore we conveniently choose $b_0 = b(t_0) \approx 0$. In sum, we have

$$s(1) = \dot{s}(1) = 1/2, \quad b(1) = 0. \tag{4.13a,b}$$

In Appendix B, we show that our model (4.12) is robust to uncertainties associated with initial value s_0 across all *We*.

Meanwhile, figure 10(*d*) shows that at $t = t_0 = 1$ the cavity has not yet reached a spherical cap shape; instead, it is a cylinder of depth $D(t_0) = D_0 \approx 0.23$ and width comparable to $\ell_0 \approx 1.7$. The associated D_0 value is close to the data at initial times reported by Engel (1967) and Elmore, Chahine & Oguz (2001). As a result, we estimate next the coefficient β in (4.11) by equating the volume of the crown at $t = t_0$, as a cylindrical wall, and that of the cavity, as a cylinder. Notably at this time, a spherical cavity has not yet formed and our cavity model discussed in § 3 does not apply. This gives

$$h_0 \ell_0 s_0 = \tfrac{1}{4}\ell_0^2 D_0, \tag{4.14}$$

where $h_0 = h(s_0, t_0)$ given by (4.11) is used as initial thickness. It immediately follows that $\beta = 0.049$, in good agreement with the value given in § 4.3.2. This reasonable match also demonstrates the robustness of the estimated initial values s_0 and ℓ_0 against measurements of all *We* previously used in the least-squares fit.

4.4.3. *Asymptotic solution*

Now we return to (4.12) and derive an asymptotic solution for s. First, substituting (4.1), (4.6) and (4.11) into (4.12a) gives a first-order ODE for $b(t)$ that can be directly integrated to generate

$$b(t) = \sqrt{\frac{4\beta t^{3/5}}{\pi s(t)} + \frac{F(z)}{t^{2/5}}}, \tag{4.15}$$

where $F(z)$ is in general an arbitrary function of z. However, the initial conditions (4.13a,b) require that $F = -8\beta/\pi$.

Meanwhile, (4.12b) can be rearranged using (4.12a) to read

$$b^2 \ddot{s} = -\frac{8}{\pi We} - \frac{b^2}{Fr} + \frac{4h(s,t)}{\pi} \left[v_s(s,t) - \dot{s} \right]^2. \tag{4.16}$$

Because $h \lesssim b(t) < 1$ and $1/Fr \ll 1$, we proceed with the limit that $b^2/Fr \to 0$. As a result, the gravitational effects are assumed to be negligible compared with the capillary effects in (4.16). This assumption is justified in Appendix B where we show the ratio between $|b^2/Fr|$ and $|8/(\pi We)|$ is small over time at least up to the time of maximum heights. Therefore, substituting (4.6), (4.11) and (4.15) into the leading-order form of (4.16) in this limit leads to the asymptotic solution

$$s(t) = \frac{4\beta t}{\pi F(z)} W_0 \left(\frac{\pi F}{4\beta} \exp \left(-\frac{25}{42\beta We} t^{7/5} + k_1 t^{-1} + k_2 \right) \right), \tag{4.17}$$

where W_0 is the principal Lambert's W function and $k_{1,2}$ are constants determined using the initial conditions (4.13a,b) again. After some simplification, we obtain

$$s(t) = -\frac{t}{2} W_0 \left(-\exp \left(-1 - \frac{25t^{12/5} - 60t + 35}{42\beta t We} \right) \right), \tag{4.18}$$

where $\beta \approx 0.044$ was determined from two independent methods in §§ 4.3.2 and 4.4.2. Further applying the limit $We \to \infty$ to (4.18) leads $s(t) \to t/2$, as expected from the evaluation of the initial values (4.14).

Our asymptotic result for the crown height $s(t)$ given in (4.18) already differs from that of the cavity depth $D(t)$ given in (3.4). The sheet height (4.18) is controlled by We, independent of Fr, while the cavity depth (3.4) depends on Fr but not on We. We discuss the physical significance of this result shortly.

4.4.4. *Maximum crown height*

Here we seek analytical expressions for the maximum crown height, s_m, and its time of occurrence, t_m, based on the explicit asymptotic solution (4.18). As we have shown, such a maximum exists only if $We > 0$ is finite, because $s(t) \to t/2$ as $We \to \infty$. Differentiating (4.18) with respect to t and requiring $\dot{s}(t_m) = 0$ yields

$$\frac{5}{t_m} - 5t_m^{7/5} + 6\beta We + 6\beta We \, W_0 \left(-\exp \left(-1 - \frac{25t_m^{12/5} - 60t_m + 35}{42\beta t_m We} \right) \right) = 0. \tag{4.19}$$

Considering that t_m is expected to be of $O(10)$ and We is large, (4.19) can be approximately solved as $We \to \infty$ after removing terms of $O(1/t_m)$ in (4.19) as

$$t_m = \left[\frac{\beta We}{10} \left(12 + 7W_0 \left(-\frac{12}{7} \exp \left(\frac{10}{7\beta We} - \frac{12}{7} \right) \right) \right) \right]^{5/7} \sim (K\beta We)^{5/7}, \tag{4.20}$$
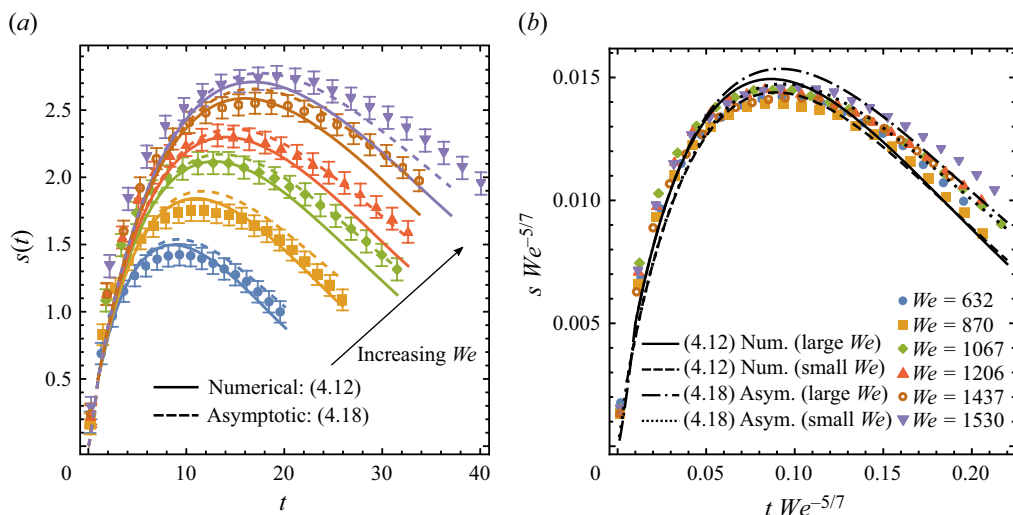
(*a*)   (*b*)

Figure 11. Evolution of the crown height s. Results for a wide range of We, as labelled in (*b*), are given. The corresponding Fr values are the same as those found in figure 5. (*a*) The $s(t)$ measurements are compared with the numerical solution to (4.12) and asymptotic theory (4.18) for each We, using solid and dashed lines, respectively. We see a good match between experiments and our model. (*b*) All results collapse well after rescaling both s and t by $We^{5/7}$. The collapsed data can be successfully captured by our model using either $We = 632$ (small) or $We = 1530$ (large).

where $K = [12 + 7W_0(-12\mathrm{e}^{-12/7}/7)]/10 \approx 0.837$.

Finally, substituting (4.20) into (4.18) produces an explicit approximation of the maximum crown height, which can be expanded as $We \to \infty$ as

$$s_m = s(t_m) \sim -\frac{1}{2}W_0\left(-\exp\left(-\frac{25K}{42} - 1\right)\right)(K\beta We)^{5/7} + O\left(We^{-2/7}\right). \qquad (4.21)$$

We find that t_m and s_m grow asymptotically as $We^{5/7}$ for large We and all Fr, provided that the assumption $b^2/Fr \ll 1$ holds. Notably, Cossali *et al.* (2004) observed similar scaling for the maximum crown height and its occurring time resulting from drop impact on a thin film. In their study, experimental measurements are fitted to the power law $s_m \propto We^p$ and $t_m \propto We^p$ with $0.65 < p < 0.75$, consistent with our exact exponent of $5/7 \approx 0.71$ derived here for deep-pool impacts.

4.4.5. *Experimental and numerical results*

Next, the asymptotic theory developed in (4.18), (4.20) and (4.21) is compared with experiments and the numerical solution of the crown height $s(t)$. Here the ODE system (4.12) with initial values (4.13*a,b*) is solved using a variable-order Runge–Kutta method.

Figure 11(*a*) gives the crown height evolution $s(t)$ for $600 < We < 1600$. In all cases, the numerical solution (4.12) and the asymptotic solution (4.18) capture the experimental data very well. As expected, the distinctions between numerical and analytical results are small until maximum height s_m is reached, beyond which the theoretical predictions start to underestimate the measurements. This deterioration is more significant as We increases. A likely explanation to this observed deviation is that we have neglected the topological changes of the rim and the associated mass loss due to droplet shedding in our reduced geometrical model.
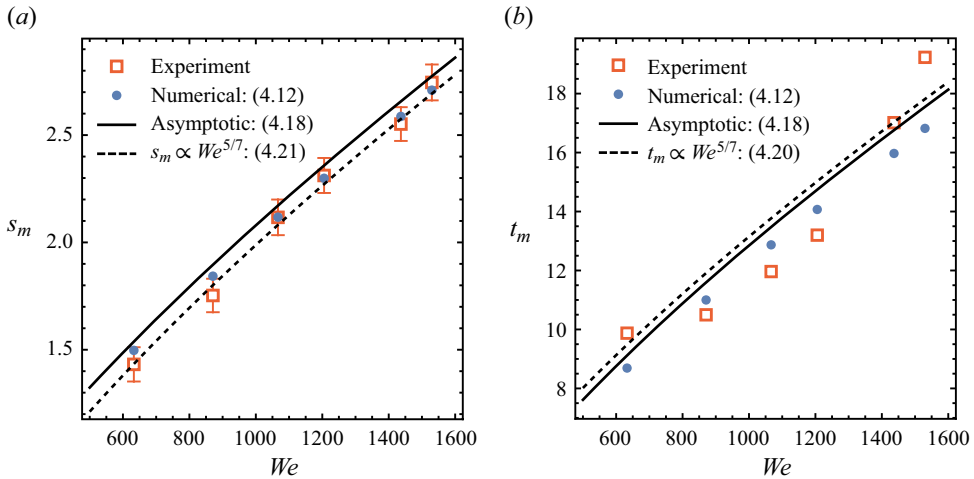
(*a*)

(*b*)

Figure 12. (*a*) Maximum crown height s_m and (*b*) its time of occurrence t_m as a function We. In both panels, the numerical solutions given by the filled circles are obtained from (4.12) with the same We and Fr values as those corresponding experiments. The asymptomatic theory of (4.18) in (*a*,*b*) are shown by the solid lines; and their large-We behaviours that grow as $We^{5/7}$, i.e. (4.21) for s_m and (4.20) for t_m, are given by the dashed lines. We clearly demonstrate that such theoretical scaling captures the measurements very well.

Although in figure 11(*a*) we observe prolonged crown growth to higher peak heights as We increases, rescaling both s and t with $We^{5/7}$, as informed by the asymptotic forms in (4.21) and (4.20), collapses the data beautifully (figure 11*b*).

Finally, the key findings of (4.20) and (4.21) are that both the maximum crown height s_m and the time t_m of its occurrence scale as $We^{5/7}$ for the entire range of Fr in the limit of large We. Figure 12 compares this theoretical finding with experiments. Comparison of s_m as a function of We among measurements, numerical solutions of (4.12) calculated using the same discrete experimental (We, Fr) parameters and the asymptotic expressions (4.18) and (4.21) that only depend on We is given in figure 12(*a*). It is established that the asymptotic relation $s_m \propto We^{5/7}$ captures the experimental data very well. The analogous comparison for t_m is shown in figure 12(*b*), where again the theoretical expression $t_m \propto We^{5/7}$ captures the experimental data very well.

Having established accuracy for both asymptotic results (3.4) and (4.18) respectively for the cavity depth and the crown height, we note that unlike the cavity that retracts because of gravitational effects acting on the liquid (see § 3.2), the crown growth up to a finite maximum height is primarily governed by surface tension effects encapsulated by finite We. Indeed (4.18) is independent of Fr, and both s_m and t_m diverge in the limit of $We \to \infty$. In sum, it is surface tension rather than gravity that stops an unbounded crown rise.

4.5. *Summary*

In this section we discuss the theoretical analysis of four quantities that characterize the crown sheet dynamics resulting from a drop-on-pool impact. According to the idealization shown in figure 4, our model entails the crown diameter ℓ, the axial flow velocity v_s, the sheet thickness h and the crown height s, not considering, for now, the destabilization of the rim, precursor of ligament formation and fragmentation into secondary droplets. We coupled the crown and cavity via the crown diameter ℓ observed to be proportional to the cavity depth. We consider the crown as a thin sheet, i.e. $h \ll \ell$, $h \ll s$, and

Crown variables	Governing equations	Analytic solutions	Experimental comparisons
Diameter, $\ell(t)$	(3.1)	(3.2a,b), (4.1)	Figure 6
Velocity, $v_s(z, t)$	(4.5)	(4.6)	Figure 8
Thickness, $h(z, t)$	(4.9)	(4.11)	Figure 9
Height, $s(t)$	(4.12)	(4.18), (4.20), (4.21)	Figures 11, 12

Table 2. Key quantities that describe the crown structure generated by a drop impact (figure 4d). A summary of their corresponding modelled equations, asymptotic solutions and validations against experimental measurements.

consequently the flow field is Q1D. We solve conservation of mass and momentum asymptotically, deriving explicit expressions that predict the corresponding measurements well, as summarized in table 2. These asymptotic results are parametrized in terms of *We* only, independent of *Fr*.

5. Summary and conclusions

In conclusion, we have addressed a sequence of events that follow the impact of a liquid droplet on a deep inviscid liquid pool, including the cavity and crown formation. We use a combined approach of experimental measurements and theoretical modelling to study the cavity–crown coupled system, with a focus on impacts with Weber numbers $500 < We < 1600$ and Froude numbers $Fr < 1000$, such that a crown splash is enabled while preventing bubble formation.

We first verify that by simplifying the cavity as an ascending sphere of expanding radius, the numerical theory of Bisighini *et al.* (2010) that describes the cavity using an ODE system successfully captures the temporal evolution of cavity depth $D(t)$ that we measure. In particular, we find that the early stage of the cavity growth follows the power law $D(t) \sim t^{2/5}$ derived as the limiting solution to the ODE system as both $We \to \infty$ and $Fr \to \infty$. Informed by such limit, we show that rescaling depth data using $We^{-1/5}D(\tau)$ as a function of dimensionless capillary time τ collapses experimental measurements well for our range of *We* and *Fr*.

However, the initial dynamics of $t^{2/5}$ growth is unable to explain the experimentally observed cavity retraction after a maximum depth is reached. To recover this behaviour, we develop an asymptotic correction to the original double limit as a function of *Fr*, so that the large-*Fr* condition is relaxed. The resulting analytical expression for $D(t)$ possesses a global maximum and reasonably captures the experimental data up to the measured maximum depth. We conclude that gravitational effects acting on the displaced liquid are the primary restoring process causing cavity retraction.

We next examine the crown structure as a double-sided cylindrical sheet with an idealized toroidal rim on top. Our key strategy is to connect the crown to the elucidated cavity evolution: the crown diameter ℓ increases at a rate proportional to the initial cavity expansion, namely $\ell \sim t^{2/5}$. The proportionality constant of this relation appears to depend on *We* and *Fr*, although only weakly, and the determination of its specific value is actually not required for our subsequent analysis aiming to elucidate the characteristic quantities of the crown sheet.

Using the key insight of coupling sheet and cavity, and applying the thin-film approximation for the sheet thickness h, we therefore obtain a Q1D flow field for the sheet, with axial velocity $v_s(z, t)$ governed by the inviscid Burger equation. The resulting

R. Dandekar, N. Shen, B. Naar and L. Bourouiba

similarity solution to v_s predicts ballistic motion of Lagrangian fluid parcels, akin to other thin sheets from drop impact, e.g. on surface of size comparable to that of the drop (Wang & Bourouiba 2017). We experimentally validate this theory using particle velocimetry where the impacting drop and the pool fluids are seeded with tracked particles in independent experiments. Subsequently, using conservation of mass and momentum for the Q1D flow we derive and validate an explicit self-similar solution for the thickness profile $h(z, t)$. The derived self-similar thickness profile captures the measured thickness for all *We* very well. The thickness is measured using a light absorption method validated in prior work (Wang & Bourouiba 2017; Si *et al.* 2024).

Similarly, by applying conservation laws over the idealized crown rim, we formulate an ODE system that couples the rim size b and the crown height s. Building on the previously obtained analytical expressions for ℓ, v_s and h, we solve the associated initial-value problem both numerically and asymptotically in the $b^2/Fr \to 0$ limit. As a result, we derive theoretical predictions of $s(t)$ in good agreement with the experimental data for the entire duration of the splash, including the initial rise and the following fall, for all *We*. From the asymptotic solution that is parametrized by *We* only, we further determine analytically the maximum crown height and its time of occurrence and we show that both scale as $We^{5/7}$. Indeed, rescaling the $s(t)$ data using $sWe^{-5/7}$ as a function of $tWe^{-5/7}$ shows excellent collapse of all measurements from different *We*. We therefore conclude that unlike the cavity whose expansion is opposed by gravitational effects, the axial crown rise is mostly opposed by surface tension effects.

Our analysis, rooted here on considering the cavity–crown coupled system, paves the way to understand the ultimate liquid fragmentation process as a result of impact and splash where secondary droplets with a distribution of sizes and speeds are ejected from the crown rim. Such fast-moving secondary droplets are critically important for contaminant and pathogen dispersal in agriculture, healthcare, and the environment (Bourouiba 2021*b*,*a*) sectors. Further, insights into a single-phase impact could be extended to impacts with multiphase liquid layers that are relevant in a wide range of applications including oil spills (e.g. Murphy *et al.* (2015), and references therein), and the climate system modelling, via ocean-atmosphere coupling upon creation of droplet residues and condensation nuclei via such deep pool splashes. Understanding the role of secondary droplets and the influence of a multiphase layer in contaminant dispersal is the subject of our ongoing work.

Author ORCIDs.

ⓘ N. Shen https://orcid.org/0000-0002-0533-8081;

ⓘ L. Bourouiba https://orcid.org/0000-0001-6025-457X.

1002 A13-24

Appendix A. Asymptotic expansion of the cavity and sheet equations

A.1. *The cavity equations for large We*

Here we perform a formal asymptotic expansion of the cavity evolution equation (3.1) in terms of small parameter $\delta \equiv 1/We \ll 1$ and derive (3.5b) as the leading-order solution for large $We \gg 1$, in the strict limit of $Fr \to \infty$. In this limit, together with the initial condition $\dot{z}(t_0) = 0$, we note again that the coupling between cavity centre z_c and radius a is weak. Therefore we proceed with the constant solution $z_c(t) = z_c(t_0)$, and consequently, $D(t) = a(t) + z_c(t_0)$. Further, we substitute the series expansion $a(t) = \sum_{n \geqslant 0} a_n \delta^n$ into (3.1a), giving

$$a_0^2 \ddot{a}_0 + \tfrac{3}{2} a_0 \dot{a}_0^2 = 0, \tag{A1a}$$

$$a_0^2 \ddot{a}_1 + 3 a_0 \dot{a}_0 \dot{a}_1 + \left(\tfrac{3}{2} \dot{a}_0^2 + 2 \dot{a}_0 \ddot{a}_0 \right) a_1 + 2 = 0, \tag{A1b}$$

at $O(1)$ and $O(\delta)$, respectively. The general solution to the leading-order equation (A1a) is given by (3.2a,b), that is,

$$a_0 = A(t - t_s)^{2/5}. \tag{A2}$$

Therefore using (A2) in (A1b) leads to the following non-divergent first-order solution:

$$a_1 = -\frac{25(t - t_s)^{6/5}}{18A^2} + A_1(t - t_s)^{2/5}, \tag{A3}$$

where both A and A_1 are general constants. Combining (A2) and (A3) we obtain the large-*We* asymptotic solution up to $O(\delta)$ as follows:

$$a(t) = A(t - t_s)^{2/5} + \frac{1}{We} \left[-\frac{25(t - t_s)^{6/5}}{18A^2} + A_1(t - t_s)^{2/5} \right] + O\left(\frac{1}{We^2} \right). \tag{A4}$$

Next, the time transformation $t = \tau/\sqrt{6/We}$ can be applied to (A4) with the dominant powers of *We* retained explicitly, producing

$$\frac{D}{We^{1/5}} \sim \frac{a}{We^{1/5}} \sim \frac{\tau^{2/5}}{6^{1/5}} - \frac{25\tau^{6/5}}{18 \times 6^{3/5} A^2} \frac{1}{We^{2/5}}. \tag{A5}$$

As $We \to \infty$, (A5) establishes that the leading-order behaviour of D as a function of capillary time τ is correctly given by (3.5b).

A.2. *Lubrication theory for the thin sheet*

In this section we derive the Q1D flow velocities given by (4.4a,b) for the rising sheet. Based on the thin-sheet assumption, i.e. $h(z, t) \ll \ell(t)$, we denote $\epsilon = H_0/L_0 \ll 1$ the small parameter that compares a characteristic sheet thickness scale H_0 with a characteristic sheet diameter scale L_0. Accordingly, we introduce the following local radial

coordinate $\tilde{r}$ for the sheet's domain described by (4.3):

$$\epsilon \tilde{r} = r - \frac{\ell}{2} \in \left(-\frac{h}{2}, \frac{h}{2} \right). \tag{A6}$$

Omitting the subscript 's' in the velocity components, the continuity equation (4.2a) thus becomes

$$\frac{\partial v}{\partial z} + \frac{1}{\epsilon} \frac{\partial u}{\partial \tilde{r}} + \frac{2u}{2\epsilon \tilde{r} + \ell} = 0. \tag{A7}$$

We seek solutions in the form of Taylor series expanded around the central ring, $\tilde{r} = 0$, as follows:

$$u = \sum_{n=1}^{\infty} u_n(z) \, (\epsilon \tilde{r})^n, \quad v = \sum_{n=0}^{\infty} v_{2n}(z) \, (\epsilon \tilde{r})^{2n}, \tag{A8a,b}$$

where the symmetry conditions $u|_{\tilde{r}=0} = 0$ and $v|_{\tilde{r}} = v|_{-\tilde{r}}$ have been applied. Substituting (A8a,b) into (A7) gives

$$u_1 + v_0' + \left[\frac{2u_1}{\ell} + 2u_2 \right] \tilde{r}\epsilon + \left[\frac{2\ell u_2 - 4u_1}{\ell^2} + 3u_3 + v_2' \right] (\tilde{r}\epsilon)^2 + \cdots = 0. \tag{A9}$$

Equation (A9) therefore demands that at leading order,

$$v \sim v_0(z), \quad u \sim u_1 \tilde{r}\epsilon = -v_0'(z) \left(r - \frac{\ell}{2} \right) \ll v. \tag{A10a,b}$$

Similarly, higher-order corrections in terms of v_n can be obtained by successively solving (A9), leading to

$$u_2 = \frac{v_0'(z)}{\ell}, \quad u_3 = -\frac{2v_0'(z)}{\ell^2} - \frac{v_2'(z)}{3\ell^2}, \quad \ldots \tag{A11a,b}$$

so the u-series in (A8a,b) can be summed. In fact, with the approximation $v = v_0$, this series converges as

$$u = -\frac{\tilde{r}\epsilon(\ell + \tilde{r}\epsilon)}{1 + 2\tilde{r}\epsilon} v_0'(z) = \frac{\ell^2 - 4r^2}{8r} v_0'(z) \ll v_0(z). \tag{A12}$$

One can readily verify that the flow field given by $v = v_0$ and (A12) satisfy the continuity equation (4.2a) exactly.

Appendix B. Robustness of the crown height model

Here, we show that the crown height model developed in § 4.4 is robust to experimentally measured initial values, and the limiting assumption of surface tension dominating gravity in (4.16) is valid.

First, we revisit the averaged initial value, $s_0 = \dot{s}_0 = 0.5$, that has been prescribed to the ODE system (4.12) for all *We*. As observed in figure 10, this approximation overestimates the measurements at low *We* but underestimates the experiments at high *We*, with margins of around 10 %. To account for this uncertainty, here we solve (4.12) (and equivalently (4.16)) numerically with a range of initial values $s(1) = \dot{s}(1) = s_0$, while fixing $b(1) = 0$ constant. Results are given for three different representative *We* and compared with the experiments in figure 13(a). Specifically, for a small $We = 630$, the region of solutions
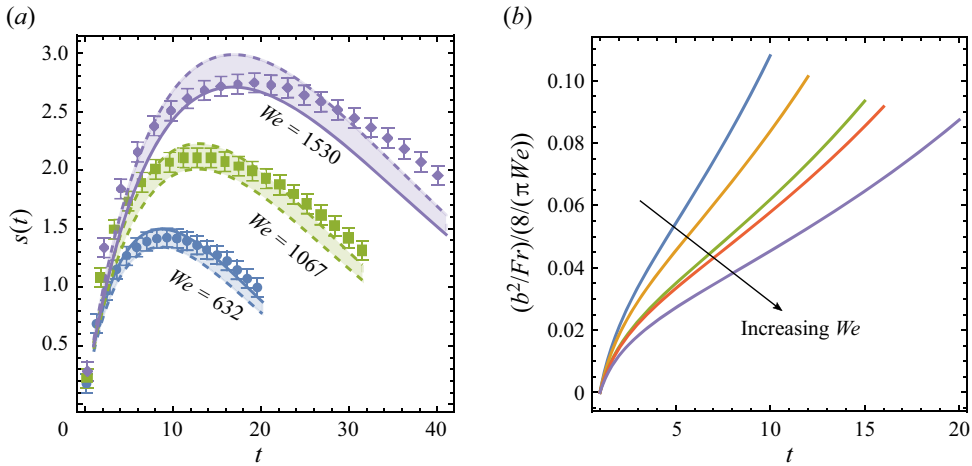
Figure 13. (*a*) Crown height, $s(t)$, shown from measurements and numerical solutions of (4.16) given by variable initial value s_0 for small, medium and large *We*. Each shaded band corresponds to 10 % variation near $s_0 = 0.5$ at a given *We*. The solid lines are obtained with $s_0 = 0.5$. The dashed lines are given by $s_0 = 0.5(1 \pm 10\,\%)$ for *We* = 630 and 1530, respectively, and $s_0 = 0.5(1 \pm 5\,\%)$ for *We* = 1070. (*b*) Ratio of the two terms that measure gravitional and surface tension effects in the numerical solutions of (4.16). Results as a function of time are given for the same *We* and *Fr* presented in figure 11.

corresponding to the initial values between $\varrho \equiv (s_0 - 0.5)/0.5 \in (-10\,\%, 0)$ is shown; for a medium *We* = 1070, the corresponding region of $\varrho \in (-5\,\%, 5\,\%)$ is given; and for a high *We* = 1530, solutions are generated using $\varrho \in (0, 10\,\%)$. In all cases, the range of solution response to initial-value uncertainties remains comparable to the experimental errors. Therefore, we have demonstrated that the crown height dynamics described by (4.12) and our reduced estimation $s_0 = 0.5$ is robust to errors/variability of s_0.

Second, we assess the accuracy of the limiting assumption made to simplify (4.16) and derive (4.18), that is, $b^2/Fr \to 0$, and particularly its implication that surface tension plays a dominant role over gravity at opposing the crown rise. In a direct comparison between the two contributions made by gravity and capillarity in (4.18), figure 13(*b*) gives the size ratio, $|b^2/Fr|/|8/(\pi We)|$, as a function of time. Here the evolution of $b(t)$ is obtained by numerically solving the full system (4.12) of finite *Fr*. We find that for all *We* (and *Fr*), the gravitational term b^2/Fr makes up less than 10 % of the capillary term $8/(\pi We)$ at least until the maximum crown height is reached. Thus, error made by taking the $Fr \to \infty$ limit for the large-*We* asymptotic solution (4.18) is small over this period, explaining the good performance of (4.18), compared with the full solution, shown in figure 11.

REFERENCES

AGBAGLAH, G., THORAVAL, M.J., THORODDSEN, S.T., ZHANG, L.V., FEZZAA, K. & DEEGAN, R.D. 2015 Drop impact into a deep pool: vortex shedding and jet formation. *J. Fluid Mech.* **764**, R1.

AGUILERA, F., MENDEZ, J., PASARO, E. & LAFFON, B. 2010 Review on the effects of exposure to spilled oils on human health. *J. Appl. Toxicol* **30**, 291–301.

ALJEDAANI, A.B., WANG, C., JETLY, A. & THORODDSEN, S.T. 2018 Experiments on the breakup of drop-impact crowns by Marangoni holes. *J. Fluid Mech.* **844**, 162–186.

ALSVED, M., BOUROUIBA, L., DUCHAINE, C., LÖNDAHL, J., MARR, L.C., PARKER, S.T., PRUSSIN, A.J. II & THOMAS, R.J. 2019 Natural sources and experimental generation of bioaerosols: challenges and perspectives. *Aerosol Sci Technol.* **54**, 1–25.

AZIZ, S.D. & CHANDRA, S. 2000 Impact, recoil and splashing of molten metal droplets. *Intl J. Heat Mass Transfer* **43**, 2841–2857.

BARKER, J. & JONES, M.V. 2005 The potential spread of infection caused by aerosol contamination of surfaces after flushing a domestic toilet. *J. Appl. Microbiol.* **99**, 339–347.

BATCHELOR, G.K. 1967 *An Introduction to Fluid Dynamics*. Cambridge University Press.

BERBEROVIĆ, E., VAN HINSBERG, N.P., JAKIRLIĆ, S., ROISMAN, I.V. & TROPEA, C. 2009 Drop impact onto a liquid layer of finite thickness: dynamics of the cavity evolution. *Phys. Rev.* E **79**, 036306.

BISIGHINI, A., COSSALI, G.E., TROPEA, C. & ROISMAN, I.V. 2010 Crater evolution after the impact of a drop onto a semi-infinite liquid target. *Phys. Rev.* E **82**, 306319.

BOUROUIBA, L. 2021*a* The fluid dynamics of disease transmission. *Annu. Rev. Fluid Mech.* **53**, 473–508.

BOUROUIBA, L. 2021*b* Fluid dynamics of respiratory infectious diseases. *Annu. Rev. Biomed. Engng* **23**, 547–577.

BOUROUIBA, L., DEHANDSCHOEWERCKER, E. & BUSH, J.W. 2014 Violent expiratory events: on coughing and sneezing. *J. Fluid Mech.* **745**, 537–563.

CASTREJÓN-PITA, A.A., CASTREJÓN-PITA, J.R. & HUTCHINGS, I.M. 2012 Experimental observation of von Kármń vortices during drop impact. *Phys. Rev.* E **86**, 045301.

COSSALI, G.E., COGHE, A. & MARENGO, M. 1997 The impact of a single drop on a wetted solid surface. *Exp. Fluids* **22**, 3463–3472.

COSSALI, G.E., MARENGO, M., COGHE, A. & ZHDANOV, S. 2004 The role of time in single drop splash on thin film. *Exp. Fluids* **36**, 888–900.

DARLOW, H.M. & BALE, W.R. 1959 Infective hazards of water-closets. *Lancet* **273**, 1196–1200.

DHIMAN, R. & CHANDRA, S. 2005 Freezing-induced splashing during impact of molten metal droplets with high Weber numbers. *Intl J. Heat Mass Transfer* **48**, 5625–5638.

EDGERTON, H. & KILLIAN, J. 1954 *Flash!: Seeing the Unseen by Ultra High-Speed Photography*. Branford.

ELMORE, P.A., CHAHINE, G.L. & OGUZ, H.N. 2001 Cavity and flow measurements of reproducible bubble entrainment following drop impacts. *Exp. Fluids* **31**, 664–673.

ENGEL, O.G. 1966 Crater depth in fluid impacts. *J. Appl. Phys.* **37**, 1798–1808.

ENGEL, O.G. 1967 Initial pressure, initial flow, and the time dependence of crater depth in fluid impacts. *J. Appl. Phys.* **38**, 3935–3940.

FAUCHAIS, P., VARDELLE, A., VARDELLE, M. & FUKUMOTO, M. 2004 Knowledge concerning splat formation: an invited review. *J. Therm. Spray Technol.* **13**, 337–360.

FEDORCHENKO, A.I. & WANG, A.-B. 2004 On some common features of drop impact on liquid surfaces. *Phys. Fluids* **16** (5), 1349–1365.

FINGAS, M. 2013 *The Basics of Oil Spill Cleanup*. Taylor & Francis.

FUDGE, B.D., CIMPEANU, R. & CASTREJÓN-PITA, A.A. 2021 Dipping into a new pool: the interface dynamics of drops impacting onto a different liquid. *Phys. Rev.* E **104** (6), 065102.

FUJIMOTO, H., OGINO, T., TAKUDA, H. & HATTA, N. 2001 Collision of a droplet with a hemispherical static droplet on a solid. *Intl J. Multiphase Flow* **27** (7), 1227–1245.

FULLANA, J.M. & ZALESKI, S. 1999 Stability of a growing end rim in a liquid sheet of uniform thickness. *Phys. Fluids* **11**, 952–954.

GERBA, C.P., WALLIS, C. & MELNICK, J.L. 1975 Microbiological hazards of household toilets: droplet production and the fate of residual organisms. *Appl. Microbiol.* **30**, 229–237.

GILET, T. & BOUROUIBA, L. 2014 Rain-induced ejection of pathogens from leaves: revisiting the hypothesis of splash-on-film using high-speed visualization. *Integr. Compar. Biol.* **54**, 974–984.

GILET, T. & BOUROUIBA, L. 2015 Fluid fragmentation shapes rain-induced foliar disease transmission. *J. R. Soc. Interface* **12**, 20141092.

VAN HINSBERG, N.P., BUDAKLI, M., GÖHLER, S., BERBEROVIĆ, E., ROISMAN, I.V., GAMBARYAN-ROISMAN, T., TROPEA, C. & STEPHAN, P. 2010 Dynamics of the cavity and the surface film for impingements of single drops on liquid films of various thicknesses. *J. Colloid Interface Sci.* **350** (1), 336–343.

HORROCKS, W.H. 1907 Experiments made to determine the conditions under which "specific" bacteria derived from sewage may be present in the air of ventilating pipes, drains, inspection chambers, and sewers. *J. R. Sanit. Inst.* **28**, 176–188.

JOHNSON, D., LYNCH, R., MARSHALL, C., MEAD, K. & HIRST, D. 2013 Aerosol generation by modern flush toilets. *Aerosol Sci. Technol.* **47**, 1047–1057.

JOSSERAND, C., RAY, P. & ZALESKI, S. 2016 Droplet impact on a thin liquid film: anatomy of the splash. *J. Fluid Mech.* **802**, 775–805.

JOSSERAND, C. & THORODDSEN, S.T. 2016 Drop impact on a solid surface. *Annu. Rev. Fluid Mech.* **48**, 365–391.

JOSSERAND, C. & ZALESKI, S. 2003 Droplet splashing on a thin liquid film. *Phys. Fluids* **15**, 1650–1657.

JUNG, S., STAPLES, S., DABIRI, J., MARSDEN, A., PRAKASH, M., DAVIS, K., SHADDEN, S., SAVIN, T., BOUROUIBA, L. & SZNITMAN, J. 2016 Research trends in biological fluid dynamics. *Tech. Rep.* Invited Report on Recent Trends in Mechanics. Publications of the US National Academies of Sciences, Engineering, and Medicine, http://sites.nationalacademies.org/cs/groups/pgasite/documents/webpage/pga_175453.pdf.

KRECHETNIKOV, R. & HOMSY, G.M. 2009 Crown-forming instability phenomena in the drop splash problem. *J. Colloid Interface Sci.* **331**, 555–559.

LHERM, V. & DEGUEN, R. 2023 Velocity field and cavity dynamics in drop impact experiments. *J. Fluid Mech.* **962**, A21.

LHUISSIER, H. & VILLERMAUX, E. 2012 Bursting bubble aerosols. *J. Fluid Mech.* **696**, 5–44.

LI, E.Q., THORAVAL, M.J., MARSTON, J.O. & THORODDSEN, S.T. 2018 Early azimuthal instability during drop impact. *J. Fluid Mech.* **848**, 821–835.

LIANG, G. & MUDAWAR, I. 2016 Review of mass and momentum interactions during drop impact on a liquid film. *Intl J. Heat Mass Transfer* **101**, 577–599.

LIOW, J.L. 2001 Splash formation by spherical drops. *J. Fluid Mech.* **427**, 73–105.

MORTON, D., RUDMAN, M. & JONG-LENG, L. 2000 An investigation of the flow regimes resulting from splashing drops. *Phys. Fluids* **12**, 747–763.

MURPHY, D.W., LI, C., D'ALBIGNAC, C., MORRA, D. & KATZE, J. 2015 Splash behaviour and oily marine aerosol production by raindrops impacting oil slicks. *J. Fluid Mech.* **780**, 536–577.

OGUZ, H.N. & PROSPERETTI, A. 1990 Bubble entrainment by the impact of drops on liquid surfaces. *J. Fluid Mech.* **219**, 143–179.

POULAIN, S. & BOUROUIBA, L. 2018 Biosurfactants change the thinning of contaminated bubbles at bacteria-laden water interfaces. *Phys. Rev. Lett.* **121**, 204502.

POULAIN, S. & BOUROUIBA, L. 2019 Disease transmission via drops and bubbles. *Phys. Today* **72**, 70–71.

POULAIN, S., VILLERMAUX, E. & BOUROUIBA, L. 2018 Ageing and burst of surface bubbles. *J. Fluid Mech.* **851**, 636–671.

PROSPERETTI, A. & OGUZ, H.N. 1993 The impact of drops on liquid surfaces and the underwater noise of rain. *Annu. Rev. Fluid Mech.* **25**, 577–602.

PUMPHREY, H.C. & ELMORE, P.A. 1990 The entrainment of bubbles by drop impacts. *J. Fluid Mech.* **220**, 539–567.

RAY, B., BISWAS, G. & SHARMA, A. 2015 Regimes during liquid drop impact on a liquid pool. *J. Fluid Mech.* **768**, 523–492.

REIN, M. 1993 Phenomena of liquid drop impact on solid and liquid surfaces. *Fluid Dyn. Res.* **12**, 61–93.

RIEBER, M. & FROHN, A. 1999 A numerical study on the mechanism of splashing. *Intl J. Heat Fluid Flow* **20**, 455–461.

ROISMAN, I.V. 2010 On the instability of a free viscous rim. *J. Fluid Mech.* **661**, 206–228.

ROISMAN, I.V., GAMBARYAN-ROISMAN, T., KYRIOPOULOS, O., STEPHAN, P. & TROPEA, C. 2007 Breakup and atomization of a stretching crown. *Phys. Rev.* E **76**, 026302.

ROISMAN, I.V., VAN HINSBERG, N.P. & TROPEA, C. 2008 Propagation of a kinematic instability in a liquid layer: capillary and gravity effects. *Phys. Rev.* E **77** (4), 046305.

ROISMAN, I.V. & TROPEA, C. 2002 Impact of a drop onto a wetted wall: description of crown formation and propagation. *J. Fluid Mech.* **472**, 373–397.

SI, X., WANG, Y., CHANDRASEKHAR, A. & BOUROUIBA, L. 2024 Light absorption method for dynamic measurement of thin liquid 894 sheet thickness and concentration fields. *Exp. Fluids* (under review).

TEAL, J.M. & HOWARTH, R.W. 1984 Oil spill studies: a review of ecological effects. *Environ. Manage.* **8**, 27–44.

THORAVAL, M.J., TAKEHARA, K., ETOH, T.G., POPINET, S., RAY, P., JOSSERAND, C., ZALESKI, S. & THORODDSEN, S.T. 2012 von Kármán vortex street within an impacting drop. *Phys. Rev. Lett.* **108**, 264506.

THORODDSEN, S.T. 2002 The ejecta sheet generated by the impact of a drop. *J. Fluid Mech.* **451**, 373–381.

TRAVERSO, G., LAKEN, S., LU, C.-C., MAA, R., LANGER, R. & BOUROUIBA, L. 2013 Fluid fragmentation from hospital toilets. American Physical Society-Division of Fluid Dynamics. Gallery of Fluid Motion. arXiv:1310.5511.

TRUJILLO, M.F. & LEE, C.F. 2001 Modeling crown formation due to the splashing of a droplet. *Phys. Fluids* **13** (9), 2503–2516.

VERNAY, C., RAMOS, L. & LIGOURE, C. 2015 Free radially expanding liquid sheet in air: time-and space-resolved measurement of the thickness field. *J. Fluid Mech.* **764**, 428–444.

WANG, A.B. & CHEN, C.C. 2000 Splashing impact of a single drop onto very thin liquid films. *Phys. Fluids* **12**, 2155–2158.

WANG, H., LIU, S., BAYEUL-LAINÉ, A.-C., MURPHY, D., KATZ, J. & COUTIER-DELGOSHA, O. 2023 Analysis of high-speed drop impact onto deep liquid pool. *J. Fluid Mech.* **972**, A31.

WANG, Y. & BOUROUIBA, L. 2017 Drop impact on small surfaces: thickness and velocity profiles of the expanding sheet in the air. *J. Fluid Mech.* **814**, 510–534.

WANG, Y. & BOUROUIBA, L. 2018 Unsteady sheet fragmentation: droplet sizes and speeds. *J. Fluid Mech.* **848**, 946–967.

WANG, Y. & BOUROUIBA, L. 2023 Non-Galilean Taylor–Culick law governs sheet dynamics in unsteady fragmentation. *J. Fluid Mech.* **969**, A19.

WEISS, A.D. & YARIN, A.L. 1999 Single drop impact onto liquid films: neck distortion, jetting, tiny bubble entrainment, and crown formation. *J. Fluid Mech.* **385**, 229–254.

WORTHINGTON, A.M. 1877 On the forms assumed by drops of liquids falling vertically on a horizontal plate. *Proc. R. Soc. Lond.* **25**, 261–272.

WORTHINGTON, A.M. 1883 On impact with a liquid surface. *Proc. R. Soc. Lond.* **34**, 217–230.

WORTHINGTON, A.M. 1908 *A Study of Splashes*. Longmans Green.

WORTHINGTON, A.M. & COLE, R.S. 1897 Impact with a liquid surface, studied by the aid of instantaneous photography. *Proc. R. Soc. Lond.* **189**, 137–148.

YARIN, A.L. 2006 Drop impact dynamics: splashing, spreading, receding, bouncing. . .. *Annu. Rev. Fluid Mech.* **38**, 159–192.

YARIN, A.L. & WEISS, D.A. 1995 Impact of drops on solid surfaces: self-similar capillary waves, and splashing as a new type of kinematic discontinuity. *J. Fluid Mech.* **283**, 141–173.

ZHANG, L.V., BRUNET, P., EGGERS, J. & DEEGAN, R.D. 2010 Wavelength selection in the crown splash. *Phys. Fluids* **22**, 122105.

ZHANG, L.V., TOOLE, J., FEZZAA, K. & DEEGAN, R.D. 2012 Evolution of the ejecta sheet from the impact of a drop with a deep pool. *J. Fluid Mech.* **690**, 5–15.